Tamaki, K., Suyehiro, K., Allan, J., McWilliams, M., et al., 1992
Proceedings of the Ocean Drilling Program, Scientific Results, Vol. 127/128, Pt. 2

78. LITHOSTRATIGRAPHY AND COMPOSITIONAL VARIATION OF NEOGENE HEMIPELAGIC SEDIMENTS IN THE JAPAN SEA[1]

Ryuji Tada[2] and Azuma Iijima[2]

ABSTRACT

The lithostratigraphy of Neogene hemipelagic sediments recovered from the Japan Sea during Leg 127 was revised to improve intersite consistency and to remove confusion stemming from diagenetic modification of the lithology through the opal-A to opal-CT transformation. Special emphasis was put on the presence and nature of dark-light cycles in revising the lithostratigraphy.

Mineral composition analysis was conducted for samples from Sites 794, 795, and 797. In addition, major element chemical composition analysis was conducted for these same sample sets from Site 794. The result of mineral composition analysis suggests that the detrital component, which consists of such minerals as quartz, plagioclase, illite, and kaolinite plus chlorite, is diluted to various degrees by biogenic silica (opal-A) and its diagenetic equivalents (opal-CT and quartz). Smectite, on the other hand, may be a diagenetic or hydrothermal alteration product of volcanic material, although more study is necessary to confirm its origin.

As a whole, vertical variation in the sediment composition is consistent with the revised lithostratigraphy and helps to characterize the redefined lithologic units quantitatively.

INTRODUCTION

During Ocean Drilling Program (ODP) Leg 127, middle Miocene to Quaternary hemipelagic sedimentary sequences were successfully recovered at all of the sites (794, 795, 796, and 797), which are located in the basinal part of the Japan Sea (Fig. 1). At each site, a similar hemipelagic sequence was recognized above the shallowest basalt, which represents acoustic basement, although the sequence at Site 796 is interrupted by numerous mass-flow deposits. In addition, lower Miocene coarse-grained sediments were penetrated below the shallowest basaltic layers at Sites 794 and 797. Core recovery was generally good except for the upper Miocene interval, where intercalated layers of hard, brittle siliceous and carbonate lithologies occur.

Six lithologic units were identified and described aboard ship (Tamaki, Pisciotto, Allan, et al., 1990). However, the criteria for identification of the lithologic units were neither selected specifically for characterization of the hemipelagic sediments nor consistent among the sites. Excessive emphasis was put on the opal-A/opal-CT boundary, which is of diagenetic origin and diachronous in nature (Tada and Iijima, 1983; Tada, 1991a). Below the opal-A/opal-CT boundary, most of the sediments encountered are highly porous and fragile, irrespective of their diagenetic silica content; thus, it was difficult to distinguish siliceous claystone from nonsiliceous claystone in many cases. Consequently, the shipboard identification and description of siliceous claystone below the opal-A/opal-CT boundary are rather ambiguous. On the other hand, it became clear after the cruise that the dark-light cycles recognized in several stratigraphic intervals reflect basin-wide paleoceanographic phenomena (Tada et al., this volume; Meredith and Tada, this volume), and the presence or absence of such cycles together with the type and intensity of bioturbation can be effectively used as criteria to distinguish the lithologic character of the hemipelagic sediments.

In realization of the described problems associated with the shipboard lithostratigraphy and because we felt that it is necessary to include criteria that characterize the depositional conditions of the hemipelagic sediments, we decided to revise the shipboard lithostratigraphy. In doing so, we paid special attention to the presence and nature of the dark-light cycles and the kind and relative amount of biogenic components. The former probably reflect bottom-water conditions, whereas the latter reflect the condition of the surface water. In this study, we also conducted X-ray-diffraction (XRD) and X-ray-fluorescence (XRF) analyses of the Neogene hemipelagic sediments to examine compositional variation through time and space and to compare the results with our revised lithostratigraphy. The results of the compositional analyses also strengthened our lithostratigraphic scheme.

REVISED LITHOSTRATIGRAPHY

To revise the lithostratigraphy, we emphasized the kind and abundances of biogenic components and the presence or absence and nature of the dark-light cycles, as well as the other sedimentary structures within the hemipelagic sediments. We also tried to make the revised lithostratigraphy compatible with the standard lithostratigraphy of northern Japan (e.g., Iijima and Tada, 1990; Iijima et al., 1988). In this paper, we numbered the revised lithologic units with Arabic numerals to distinguish them from the units identified with Roman numerals that are described in the *Initial Reports* (Tamaki, Pisciotto, Allan, et al., 1990).

Description of Lithologic Units

Unit 1: Dark- and Light-Banded Silty Clay

Unit 1 is basically identical to Unit I although the boundary with Unit II is slightly adjusted for consistency among the sites.

Unit 1 is characterized by a decimeter- to meter-scale alternation of dark (olive black to olive gray) and light (greenish gray to light gray) silty clay to clay with abundant intercalations of thin ash layers. The dark layers are rich in organic matter and pyrite, contain fine to coarse laminations, and have sporadic sharp bases and gradational tops with normal (i.e., lightening upward) color grading. The light layers are poor in organic matter and pyrite and are homogeneous, although distinct burrows are rare to absent, especially in the upper half of Unit 1. Some light layers have thin (<2 cm) intercalations of dark greenish gray silty clay beds that show normal color grading. Some of the dark and light layers contain abundant calcareous and/or siliceous microfossils (Tada et al., this volume). The siliceous microfossils are more abundant at the northern sites. At Sites 795 and 796, located in the northern part of the Japan Sea, dropstones are found within silty clay at several stratigraphic levels (Fig. 2). The dropstones are as large as 5 cm in the long diameter, well rounded, and composed primarily of andesitic volcanic rocks (Pl. 1). At Site 796, thin layers

[1] Tamaki, K., Suyehiro, K., Allan, J., McWilliams, M., et al., 1992. *Proc. ODP, Sci. Results*, 127/128, Pt. 2: College Station, TX (Ocean Drilling Program).

[2] Geological Institute, University of Tokyo, 7-3-1 Hondo, Tokyo 113, Japan.

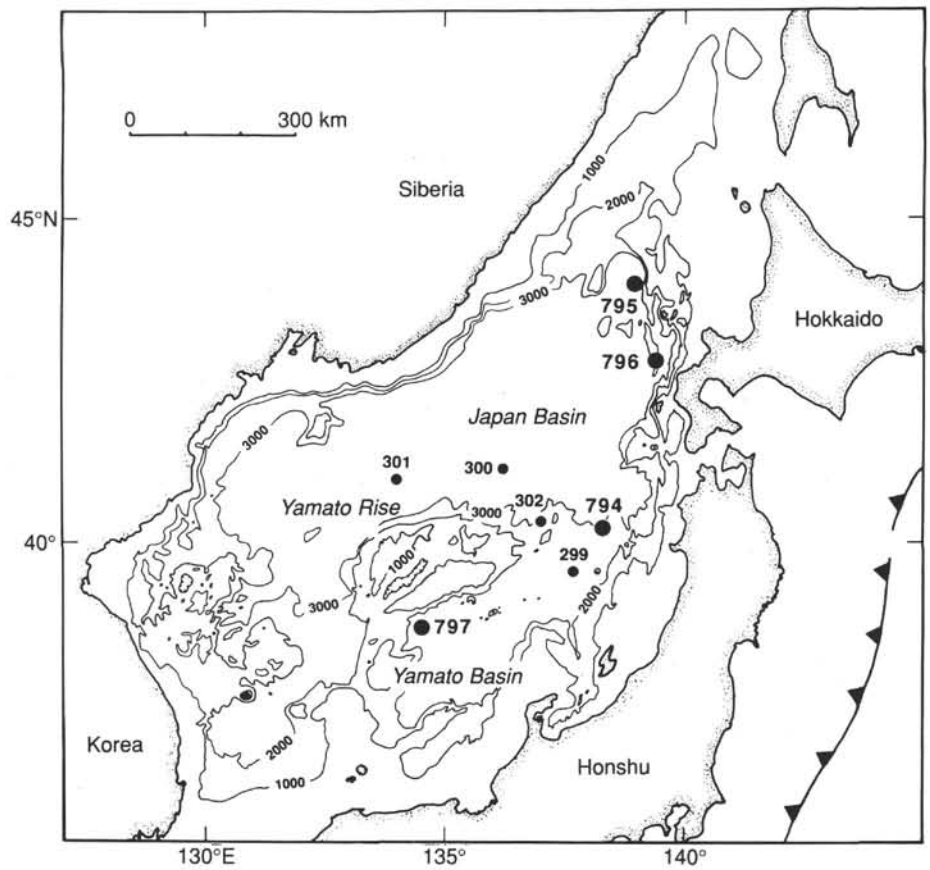

Figure 1. Map of the Japan Sea showing the location of Sites 794, 795, 796, and 797 drilled during Leg 127. Bathymetric contours in meters.

of volcaniclastic sand of possible turbidite origin occur in the lower part of Unit 1, below 63 m below seafloor (mbsf) (Fig. 2).

Unit 1 is further divided into two subunits. Subunit 1A is characterized by numerous and distinct dark layers and rare bioturbation, whereas Subunit 1B is characterized by sparse and distinct dark layers and common bioturbation, which becomes more intense downsection. The boundary between Subunits 1A and 1B is at approximately 43.8 (Section 127-794A-5H-6, 80 cm), 64.6 (Section 127-795A-7H-6, 50 cm), 41.8 (Section 127-796A-6H-l, 55 cm), and 59.8 mbsf (Section 127-797B-7H-5, 75 cm).

The boundary between Unit 1 and Unit 2 is defined by the deepest appearance of recognizable dark layers in Unit 1. It is at approximately 77.0 (Section 127-794A-9H-3, 85 cm), 142.2 (Section 127-795A-15H-CC, 20 cm), ~78 (Section 127-796A-11X-1. 0 cm), and 112.4 mbsf (Section 127-7-13H-2, 55 cm). The boundary coincides with the stratigraphic position from which organic carbon content decreases abruptly downsection to below 1 wt% (Tamaki, Pisciotto, Allan, et al., 1990). It also corresponds roughly to the position of a sudden increase in diatom abundance downsection. Based on shipboard smear slide analysis, diatom abundance increases sharply from 77 to 95 mbsf at Site 794, from 107 to 142 mbsf at Site 795, from 58 to 90 mbsf at Site 796, and from 112 to 118 mbsf at Site 797.

Unit 2: Diatom Ooze and Diatomaceous Clay

Unit 2 is basically identical to Unit II at Site 797, but differs from Unit II at Sites 794, 795, and 796.

Unit 2 is characterized by greenish gray to grayish olive green, heavily bioturbated and mottled diatom ooze, clayey diatom ooze, and diatomaceous clay and their diagenetic equivalents, such as porcellanite and siliceous claystone. The lithology is nearly homogeneous throughout, except for sporadic intercalations of yellowish brown carbonate layers at Sites 794, 795, and 797. At Site 796, the accumulation of diatomaceous clay is interrupted by numerous volcaniclastic sand layers. Dropstones were found at several stratigraphic levels in the upper to middle part of this unit at Site 795 (Fig. 2).

The diatom content of Unit 2, based on shipboard smear slide analysis, is generally between 40% and 80% at Sites 794, 795, and 797, whereas it is lower (between 20% and 50%) at Site 796.

The boundary between Unit 2 and Unit 3 is defined by the shallowest occurrence of the distinct dark-light cycles of Unit 3 and the decrease in lightness of sediment color in Unit 2 downsection. The boundary is situated approximately at 246 (Section 127-794A-27X-1), 395 (Section 127-795B-4R-1). 196 (Section 127-796A-23X-2), and 224 mbsf (Section 127-797B-25X-1). The boundary coincides with the stratigraphic level at which organic carbon content suddenly increases downsection at Sites 794, 795, and 797 (Tamaki, Pisciotto, Allan, et al., 1990). It also corresponds roughly to the position of the sudden decrease in biogenic or diagenetic silica content downsection.

Shipboard smear slide analysis shows that diatom abundance decreases sharply from 216 to 270 mbsf at Site 794, from 182 to 195 mbsf at Site 796, and from 219 to 229 mbsf at Site 797. These changes occur well above the opal-A/opal-CT boundary and thus represent primary depositional signals rather than diagenesis. In contrast, the abrupt decrease in diatom abundance at 325 mbsf at Site 795 is caused by the dissolution of diatom frustules and corresponds to diagenetic silica phase transformation from opal-A to opal-CT (Tada and Iijima 1983). The results of shipboard and shore-based XRD analyses,

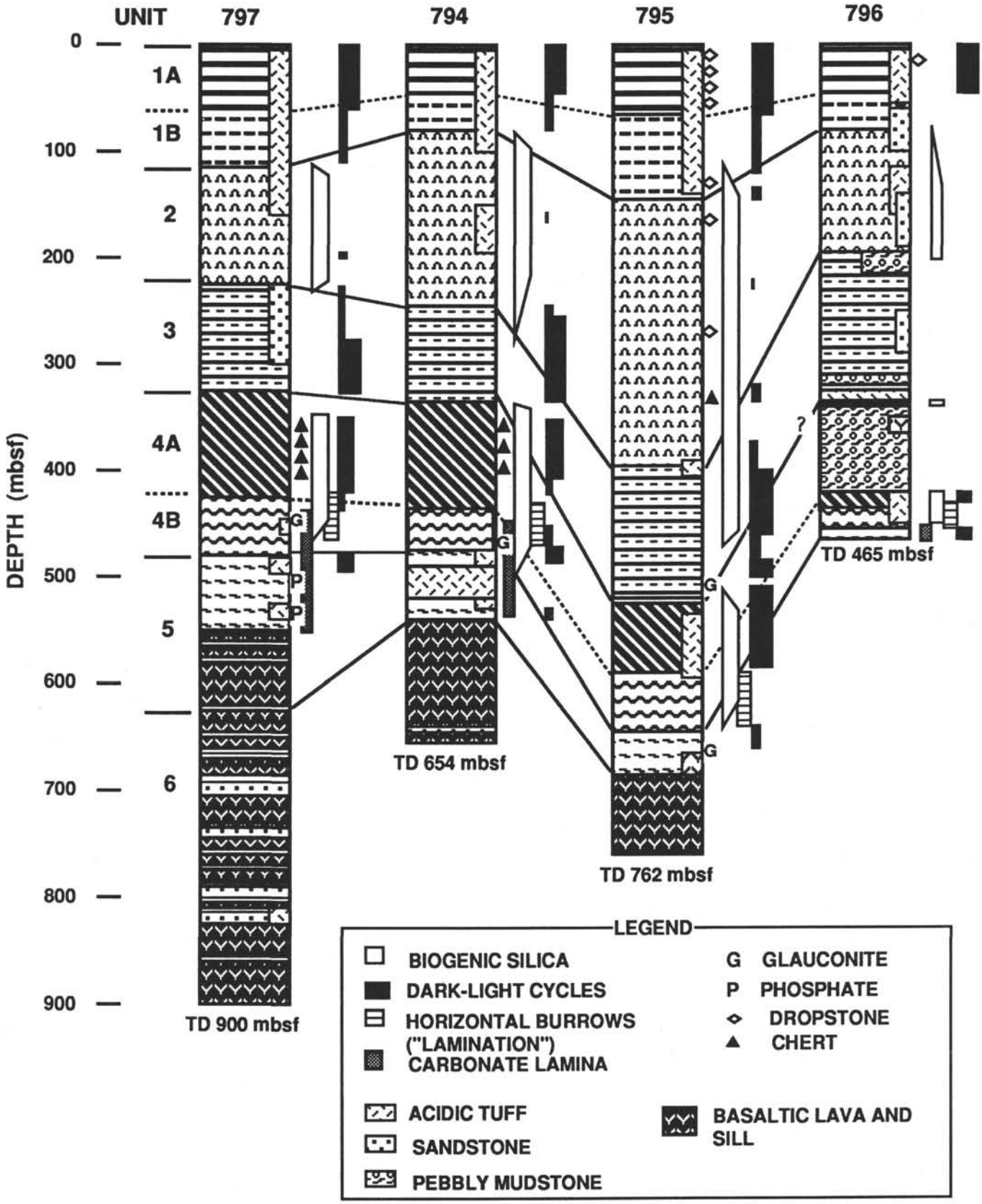

Figure 2. Stratigraphic sections and correlation of the revised lithologic units among sites drilled during Leg 127. Minor lithology is also shown.

which will be discussed later, show that the sediments immediately below 325 mbsf at Site 795 contain opal-CT in amounts that are not so different from that of opal-A in the sediments immediately above 325 mbsf. Thus, we consider the abrupt decrease in diatom abundance at 325 mbsf to be to due to the opal-A to opal-CT transformation and not representative of any change in biogenic silica content at the time of deposition.

Unit 3: Dark-Light Diatomaceous or Siliceous Silty Clay and Silty Clay

Unit 3 is different from Unit III at all four sites.

Unit 3 is composed of diatomaceous silty clay and silty clay and their diagenetic equivalents, such as silty claystone, siliceous silty claystone, and porcellanite. The sediments show decimeter- to meter-scale cycles of dark (olive gray to olive black) to light (greenish gray). The dark layers are generally 5 to 30 cm thick and faintly laminated to weakly bioturbated, mostly by *Chondrites*-like burrows, whereas the light layers are 30 to 100 cm thick and moderately to heavily bioturbated by various types of horizontal and oblique burrows with a larger diameter (Pl. 2). The pattern of vertical change in the type and size of the burrows and intensity of the bioturbation is similar to that described by Savrda and Bottjer (1986, 1989) and should represent change in the bottom-water oxygenation level. The organic carbon content is high in the dark layers of Unit 3, especially at Sites 794 and 797 where it reaches as much as 6 to 8 wt%. Intercalated yellowish brown carbonate concretions and layers are common, especially in the lower half of this unit.

Based on the shipboard smear slide observation, the silty clays of Unit 3 are coarser grained compared with the sediments in Unit 2 and rich in reworked materials such as fragments of foraminifer shells, sponge spicules, radiolarian skeletons, and glauconite pellets, especially at Site 797. At Site 797, bioclastic sand layers, as thick as 3 cm, are commonly intercalated in the upper half of Unit 3 (above 299 mbsf). Scattered glauconite pellets were found at the basal part of this unit at Site 795.

At Site 796 many of the aforementioned sedimentary features are not observed as a result of the numerous interruptions of hemipelagic sedimentation by volcaniclastic sand and pebbly mudstone deposition.

The bottom of Unit 3 is defined by the deepest occurrence of the characteristic distinct dark layers, which is at 333 (Section 127-794A-36X-1), 525 (between Cores 127-795B-17R and 127-795B-18R), and 327 mbsf (Section 127-797B-35X-4). At Site 796, the bottom of Unit 3 is positioned tentatively at 340 mbsf (between Cores 127-796B-20R and 127-796B-21R), where siliceous claystone with dark-light cycles changes downsection into pebbly mudstone.

Unit 4: Chert and Siliceous Claystone

Unit 4 is completely different from Unit IV at all four sites.

Unit 4 is characterized by the rhythmic alternation of darker (greenish black) chert to porcellanite and lighter (greenish gray) claystone to siliceous claystone in the upper part (Subunit 4A) and intermediate to light (greenish gray to olive gray) siliceous claystone in the lower part (Subunit 4B). The rocks in this unit are generally more siliceous, finer grained, and lighter in color than those in Unit 3.

Within Subunit 4A, core recovery was poor at Sites 794 and 797 because of the alternation of brittle cherty layers and ductile siliceous claystone layers. The poor recovery made it difficult to perform a detailed visual observation at these sites. However, relatively good recovery was obtained at Site 795.

At Site 795, the siliceous claystone of Subunit 4A is lighter in color than that of Unit 3, but still shows faint dark-light cycles. Darker layers, 5 to 30 cm thick and more siliceous and weakly bioturbated (mostly by *Chondrites*- and *Zoophycos*-like burrows), alternate with lighter layers that are 30 to 100 cm thick, less siliceous, and moderately to heavily bioturbated (by a variety of horizontal and oblique burrows). At Site 795 acidic to intermediate, vitric to vitric crystal tuff layers, as thick as 50 cm, are intercalated in Subunit 4A.

Formation microscanner (FMS) images from Sites 794 and 797 also suggest that this subunit is characterized by the rhythmic alternation of 5- to 50-cm-thick bedded layers with a high resistivity and 10- to 100-cm-thick homogeneous layers with a low resistivity. Judging from the small amount of rock fragments recovered from these sites, the high-resistivity layers apparently correspond to chert whereas lower resistivity layers correspond to siliceous shale. Carbonate layers are probably rare within Subunit 4A because almost no carbonate rock fragments were recovered.

The boundary between Subunits 4A and 4B is defined by the disappearance of faint dark-light cycles and the appearance downsection of parallel lamination with common horizontal flattened burrows (Pl. 3). These burrows were described simply as laminations aboard ship. The boundary between Subunits 4A and 4B is located at 434 (between Cores 127-794B-14R and 127-794B-15R), 587 (between Cores 127-795B-23R and 127-795B-24R), and 427 mbsf (between Cores 127-797B-45X and 127-797B-46X). At Site 796, we tentatively located the boundary at 433 mbsf (Section 127-796B-30R-2), where faint, wispy laminations and horizontal burrows appear downsection.

Subunit 4B is characterized by partly parallel-laminated, light siliceous claystone with abundant horizontal flattened burrows. Scattered glauconite pellets were found in the lower part of this subunit at Sites 795 and 797, and a distinct glauconite bed, approximately 20 cm thick, was found at the base of Subunit 4B at Site 794 (Pl. 4). Carbonate nodules are common in this subunit at Sites 794 and 795, and wispy carbonate laminae were found in the lower part of Subunit 4B at Sites 794 and 797.

The bottom of Unit 4 is defined by the disappearance of parallel lamination and the occurrence of dark-light cycles downsection approximately at 475 (Section 127-794B-19R-2), 645 (Section 127-795B-30R-1), 438 (Section 127-796B-31R-2), and 480 mbsf (Section 127-797B-51X-3).

Unit 5: Claystone with Carbonate Nodules and Stringers

Unit 5 is modified significantly from Unit V.

Unit 5 consists of dark (olive gray) claystone with carbonate stringers and nodules. Indistinct dark-light cycles are present in the upper part of this unit. The carbonate nodules and stringers are light olive gray to yellowish brown and rather soft and porous. The diameter of the nodules rarely exceeds 1 cm and the surrounding claystone shows compactional draping around the nodules. Stringers are 0.2 to 1 cm thick, wavy, and discontinuous, and some are cut by burrows (Pl. 5). Both the nodules and stringers tend to occur within dark layers. Horizontal burrows occur in this unit.

Acidic to intermediate vitric to vitric crystal tuff layers, as much as 28 m thick, are intercalated within Unit 5 only at Sites 794 and 797. The tuff is generally bentonitic and was called blue tuff in the shipboard description. Judging from the sedimentary structures, such as normal and reverse grading, parallel and cross lamination, and bottom scour, the tuff layers are considered to be subaqueous pyroclastic flow deposits.

The lowest part of Unit 5 was intruded by basaltic sills at 544 mbsf at Site 794 (Section 127-794B-26R-2), and the exact boundary with Unit 6 was not observed. At Site 795, Unit 5 is underlain by basaltic brecciated lava at 684 mbsf (Section 127-795B-34R-1). At Site 796, the bottom of Unit 5 was not penetrated and the hole was terminated at 464.9 mbsf. At Site 797, brecciated basaltic lava flows and sills are intercalated in the lower part of this unit and the lowest part of Unit 5 was observed between sills at a depth of 618 mbsf (Section 127-797C-15R-1). Silicified tuffaceous claystone and conglomerate were recovered between basaltic lavas and sills (Sections 127-797C-9R-1 to 127-797C-15R-1). The appearance of the claystone found between

the sills is similar to that of Unit 5, and the conglomerate consists of well-rounded pebbles of siliceous claystone with a siliceous clay matrix. For these reasons, we include the claystone and conglomerate in Unit 5.

Unit 6: Sandstone, Siltstone, and Silty Claystone

Unit 6 is basically the same as Unit VI and was encountered only at Sites 794 and 797.

Unit 6 is characterized by the rhythmic repetition of sandstone, siltstone, and silty claystone. The sandstone is light gray in color and medium to fine grained. The abundant sedimentary structures include bottom scours, load casts, normal graded bedding, parallel lamination, cross lamination, flame structures, rip-up clasts, and rare vertical burrows. Carbonaceous woody fragments are concentrated in the dark laminae. Bottom scour and normal grading are common in the coarser and thicker sandstone layers. The sand layers are a few millimeters to several decimeters thick, and tend to be thicker in the middle and lower part of the unit at Site 797. Sandstone generally grades upward into siltstone.

The siltstone is brownish gray to brownish black in color and shows sedimentary structures such as normal size and color grading, planar parallel lamination, rip-up clasts, and burrows. The planar parallel lamination is generally faint and composed of slightly lighter colored sandy laminae. The rip-up clasts are brownish black, angular, flattened parallel to the bedding, and a few centimeters long on the cut surface. They are difficult to distinguish from burrows in many cases. Burrows are not common and tend to be restricted to the upper part of the siltstone layers. The thickness of the siltstone layers ranges from a few centimeters to several decimeters, and the layers tend to be thicker in the middle to lower parts of Unit 6 at Site 797. Carbonaceous fragments are common in the siltstone.

The silty claystone is olive gray in color, less than a few centimeters thick, and slightly to moderately bioturbated. Occurrences of the silty claystone are common, and the layers are slightly thicker in the upper part and thinner toward the middle and lower parts of Unit 6 at Site 797.

The sandstone and siltstone are generally tuffaceous especially at Site 794 and in the middle part of Unit 6 at Site 797. At Site 797, the sandstone and siltstone in the lower part of the unit are less tuffaceous and darker colored because of the abundant carbonaceous material and increased content of quartz, feldspar, and biotite grains.

The base of Unit 6 was not penetrated during Leg 127. The deepest occurrences of Unit 6 are at 646 (Section 127-794C-13R-2) and 956 mbsf (Section 127-797C-41R-CC).

Correlation of Lithologic Units among Sites

Units 1 through 5 were identified at all four sites drilled during Leg 127. Thus, lithostratigraphic correlation is possible (Fig. 2). Furthermore, it became clear that even layer-by-layer correlation is possible among the sites, especially for Subunit 1A and Unit 4.

Based on visual inspection of the core photographs, Tada et al. (this volume) found that most of the dark layers in Subunit 1A are correlatable among Sites 794, 795, and 797 and that deposition of these dark layers was nearly synchronous because they maintain a parallel relationship with marker ash layers and paleomagnetic boundaries. In the same manner, layer-by-layer correlation is possible for the sediments of Unit 4 between Sites 794 and 797 using FMS images (Meredith and Tada, this volume) and microspherically focused log profiles (Fig. 3). The high-resistivity–low-resistivity cycles observed on the FMS images probably correspond to dark siliceous–light argillaceous cycles. Because such cycles probably represent nearly synchronous, basin-wide fluctuations in paleoceanographic conditions, correlation of the FMS images tightly constrains the construction of an intersite-consistent age model.

The age of the sediments at the four sites was estimated mainly from the biostratigraphic data. Above the opal-A/opal-CT boundary, siliceous microfossils are well preserved and the sediment age is relatively well constrained, mainly by the diatom biostratigraphy. However, below the opal-A/opal-CT boundary, diatoms are almost entirely dissolved, except for a few cases of preservation within carbonate nodules. Thus, the sparse occurrence of poorly preserved nannofossils and planktonic foraminifers together with the rare occurrence of diatoms preserved within carbonate nodules give restricted and poorly constrained age information. For this reason, the sediment age for the lower half of the sedimentary sequence presented in the *Initial Reports* (Tamaki, Pisciotto, Allan, et al., 1990) is far from conclusive.

For example, layer-by-layer correlation for Unit 4 between Sites 794 and 797 based on FMS images (Meredith and Tada, this volume) is inconsistent with the age model constructed aboard ship. If we trust the layer-by-layer correlation shown in Figure 3, then either the age of Units 4 and 5 suggested in the *Initial Reports* for Site 794 is too young or the age suggested for Site 797 is too old by 1.5 m.y. New nannofossil data suggest that the upper part of Unit 4 at Site 794 may be approximately 1.5 m.y. older (Rahman, this volume). However, inconsistencies remain among biostratigraphic datum planes based on nannofossils, planktonic foraminifers, and diatoms and the layer-by-layer correlation of FMS images. For this reason, we decided to suspend our discussion on the ages of our revised lithologic units and their differences among the sites.

COMPOSITIONAL VARIATION

Samples and Methods

Sample Preparation and Storage

Sediment samples (5 cm^3) from Sites 794, 795, and 797 were desalted twice with approximately 80 mL of deionized water and centrifuged. Samples were then dried at 60°C for 2 to 3 days and powdered with an agate mortar. Samples from Site 794 were processed within 2 months after the cruise, whereas samples from Sites 795 and 797 were stored for 14 months before processing. Storing the moist samples at room temperature for more than a year caused the oxidation of pyrite and the precipitation of gypsum and jarosite in several samples. It is possible that organic matter was also oxidized. For this reason, we did not analyze carbon and sulfur for the samples from Sites 795 and 797.

XRD Analysis

XRD analysis was conducted for all samples from all four sites. Semiquantitative mineral analysis of the bulk samples was performed using a Rigaku-Denki Geigerflex 4012 X-ray diffractometer. Powdered samples were mounted on a glass holder and X-rayed from 40° to 2° 2θ CuKα. Measurements were made at 30 kV and 15 mA with a slit system of 1°:0.15°:1°, scanning speed of 4°/min, and a time constant of 1 s. A control sample was run twice every day, at the beginning and the end of the measurement session, to check the change in recent conditions. Conditions were stable during the entire measurement program. The peak-height reproducibility is better than ±5%.

Opal-A peak height was determined by the height of its hump at 22° relative to the background level, which is defined as the average of the intensities at 16° and 39°. As for opal-CT, its peak area was determined instead of peak height because its crystallinity gradually increases during diagenesis (Murata and Nakata, 1974). We defined the area as peak height (at 21.6° to 21.9°) multiplied by the width of the peak taken at the height midpoint.

Detailed identification of the clay minerals was not conducted because of time limitations. The peak at approximately 12.4° was

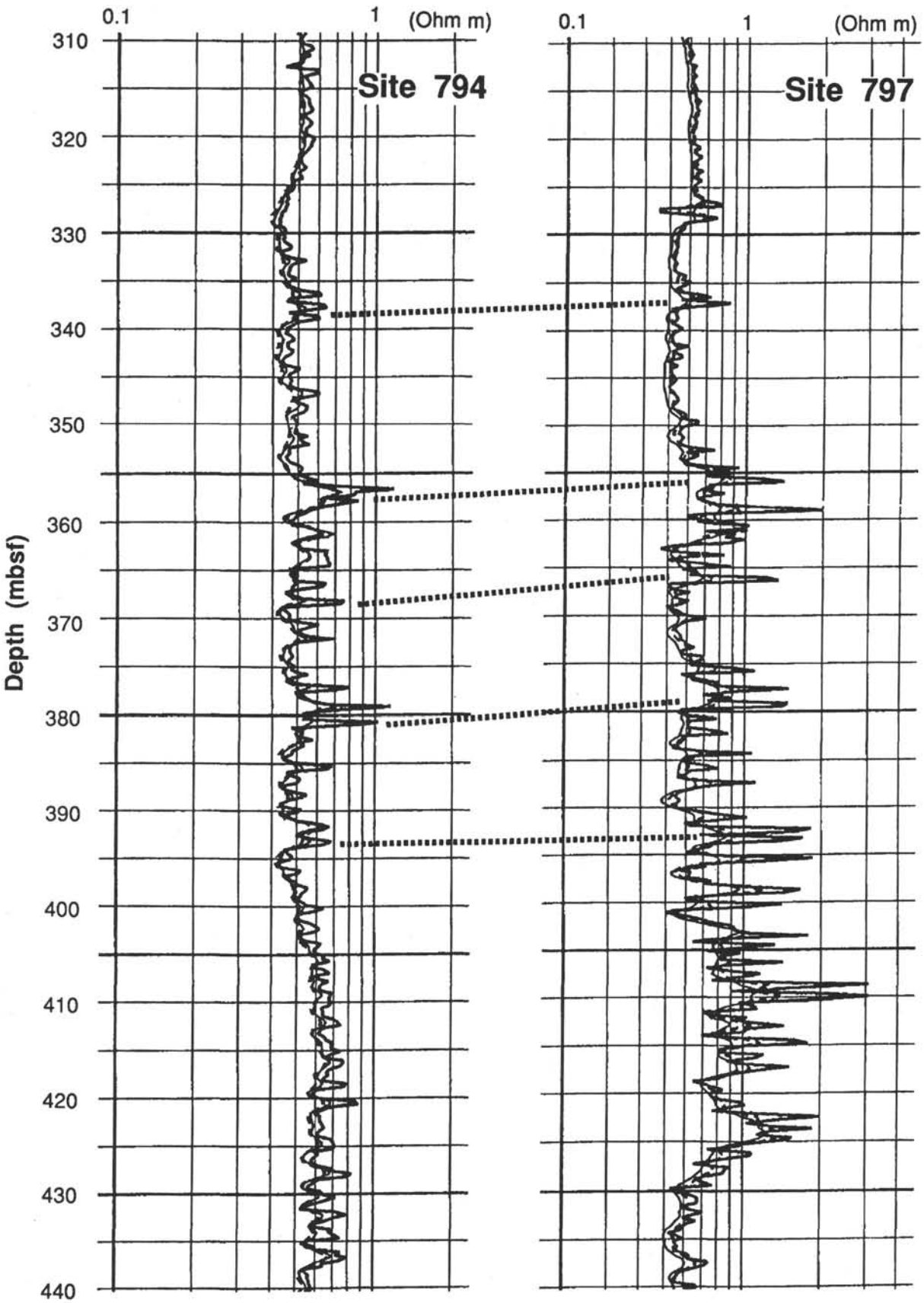

Figure 3. Correlation of microspherically focused log profiles between Sites 794 and 797. Even a layer-by-layer correlation is possible between the two sites (see Meredith and Tada, this volume).

tentatively identified as kaolinite plus chlorite, the peak at 8.8° as illite, and a rather broad peak at about 6° tentatively as smectite. Because the second peak of chlorite may overlap with the smectite peak and the crystallinity of smectite may change during diagenesis, the peak height of smectite poorly represents the amount present. It should be stressed that because of these limitations the results of clay mineral identification and semiquantification are only preliminary.

XRF Analysis

XRF analysis was conducted for samples from Site 794 only, because our XRF machine suffered mechanical difficulties just after we finished analysis of the Site 794 samples.

Major element composition was analyzed by XRF using a Rigaku-Denki IKF 3064. The analysis was performed on fused disk samples using a chromium tube at 45 kV and 30 mA. To prepare a fused disk, 1 g of powdered sample dried at 100°C was mixed with 5 g of lithium borate, which was also dried at 100°C. Ignition loss of the sample was calculated from weight loss during the fusion process corrected for weight loss attributable to the flux itself. The effect of sample to flux ratio change due to ignition loss was also corrected for by assuming a linear relationship between the sample concentration within a disk and the peak intensity. Details of the methodology and precision for major element analysis are described in Matsumoto and Urabe (1980).

Carbon and Sulfur Analyses

Total carbon and organic carbon contents were analyzed using a Leco WR-12 carbon determinator. Approximately 0.1 g of powdered sample was oxidized at 1500°C for 55 s, and the evolved CO_2 gas was measured. For the determination of organic carbon, 0.1 g of powdered sample was treated with 10% HCl for 24 hr, and then dried at 60°C within a permeable crucible. Carbonate carbon content was calculated by total carbon minus organic carbon. Precision is better than ±0.02%.

Total sulfur was analyzed using a Leco solid-state automatic sulfur determinator. Approximately 0.1 g of powdered sample was oxidized at 1650°C for 15 min, and the evolved SO_2 gas was titrated. Precision is better than ±0.05%.

Results of Analyses

Mineral Composition at Sites 794, 795, and 797

The results of XRD analysis are listed in Table 1. In general, Neogene and Quaternary fine-grained hemipelagic sediments from the Japan Sea are composed mainly of quartz; plagioclase; clay minerals such as smectite, illite, kaolinite, and/or chlorite; opal-A (biogenic silica); opal-CT; and pyrite. Calcite, dolomite and possible rhodochrosite (which we describe simply as carbonate in this paper), clinoptilolite, and analcime occur in significant amounts in several samples. Gypsum and jarosite are also present in samples from Sites 795 and 797, but because they are most likely alteration products, only their presence is noted in Table 1. There may be other minor minerals that were not identified by the XRD analysis of bulk samples.

Figures 4 through 6 show the vertical variation in peak intensity of some of the minerals at Sites 794, 795, and 797, respectively. It is obvious from the figures that the peak heights of plagioclase and illite are high and variable within Unit 1, whereas their peaks are generally low in Units 2, 4, and 5 and slightly higher in Unit 3 especially at Site 794. The peak height of kaolinite plus chlorite, although not shown in the figures, has a vertical profile similar to that of illite. The quartz peak height shows a similar profile to those of these minerals to the depth where the opal-CT to quartz transformation takes place. Below this boundary, the quartz peak height increases significantly.

The peak heights of quartz (above the opal-CT/quartz boundary), plagioclase, illite, and kaolinite plus chlorite show a positive correlation with one another. Illite and kaolinite plus chlorite show a clear positive correlation ($r^2 = 0.71$) with an intercept near zero (Fig. 7A). No obvious difference in their relation among the three sites suggests that their ratio is roughly constant at all three sites. The quartz and plagioclase relation is also similar, thus keeping roughly the same ratio at the three sites (Fig. 7B). On the other hand, the plagioclase (or quartz) and illite (or kaolinite plus chlorite) relation differs slightly among the three sites. Namely, plagioclase tends to be enriched relative to illite at Site 795, compared with Sites 794 and 797 (Fig. 7C). It should be mentioned that no significant vertical change in the peak ratios among these minerals is obvious at the three sites.

Smectite seems to show a different behavior from the minerals described previously. Smectite peak height is low in Units 1, 2, and 4 and tends to be high in Units 3 and 5. Figure 7D shows that the smectite peak height does not correlate with the illite peak height nor does it correlate with quartz, plagioclase, and kaolinite plus chlorite.

The opal-A peak is present in various intensities above 296.7 mbsf at Site 794, 325.5 mbsf at Site 795, and 300.4 mbsf at Site 797. Its peak height is generally low in Unit 1, increases sharply near the Unit 1/2 boundary, and fluctuates within Unit 2 at all the three sites. The peak height starts decreasing near the Unit 2/3 boundary at Sites 794 and 797, whereas opal-A disappears within Unit 2 at Site 795. The opal-A peak height decreases in the upper part of Unit 3 and disappears near the base of Unit 3 at Sites 794 and 797.

The opal-CT peak replaces the opal-A peak (broad hump) downsection. From the combined data from samples examined in this study and those examined aboard ship, the shallowest occurrences of opal-CT are at 303.3 (Sample 127-794A-33X-1, 3 cm), 325.2 (Sample 127-795A-35X-6, 5 cm), and 298.8 mbsf (Sample 127-797B-32X-5, 88 cm). At Site 794, opal-CT occurs from the lower part of Unit 3 to the upper part of Unit 4. In the lower part of Unit 3, its occurrence is sporadic and its peak area is small, whereas it occurs continuously and its peak area is large in the upper part of Unit 4. At Site 795, opal-CT occurs from the lower part of Unit 2 to the upper part of Unit 3. In the lower part of Unit 2, it occurs continuously, and its peak area is moderate to large, whereas its peak area is highly variable in the upper part of Unit 3. At Site 797, opal-CT occurs in the upper part of Unit 4, where its peak area is highly variable.

Below the shallowest occurrence of opal-CT, its peaks gradually become sharp and finally disappear, which corresponds to the opal-CT to quartz transformation. When shipboard XRD data are included, opal-CT disappears and quartz intensity increases significantly within relatively narrow intervals between 386.3 (Sample 127-794B-10R-1, 72 cm) and 395.8 mbsf (Sample 127-794B-11R-1, 57 cm), 466.1 (Sample 127-795A-11R-3, 140 cm) and 473.1 mbsf (Sample 127-795A-12R-7, 24 cm), and 428 (Sample 127-797B-46R-1, 140 cm) and 438.2 mbsf (Sample 127-797B-47R-2, 62 cm).

Quartz intensity increases significantly just below the deepest occurrence of opal-CT at all three sites (Figs. 4 through 6). Below the deepest occurrence of opal-CT, the quartz peak height is generally high within Unit 4 and rather low within Unit 5. At Site 794, the quartz peak becomes high at the base of Unit 5. Clinoptilolite appears at approximately the same depth as that of opal-CT and disappears at approximately the same or a slightly deeper depth than the deepest occurrence of opal-CT. When the shipboard XRD results are included, its shallowest and deepest occurrences are at 297.5 (Sample 127-794A-32X-3. 100 cm) and 386.3 mbsf (Sample 127-794B-10R-1, 72 cm), 337.1 (Sample 127-795A-37X-1, 15 cm) and 693.7 mbsf (Sample 127-795B-34R-1, 22 cm), and 298.8 (Sample 127-797B-32X-5, 88 cm) and 428 mbsf (Sample 127-797B-1, 140 cm), respectively. It is interesting to note that although opal-CT and clinoptilolite occur within a similar depth interval, their occurrence and abundance within that interval tend to be mutually exclusive.

Major Element Chemical Composition at Site 794

The results of chemical composition analyses, including carbon and sulfur, are listed in Table 2. In general, the vertical profile of SiO_2 varies in an opposite manner than that of most other elements.

Table 1. XRD analysis of bulk samples from Sites 794, 795, and 797.

Core, section, interval (cm)	Depth (mbsf)	Quartz (cps/10)	Plagioclase (cps/10)	Illite (cps/10)	Koalinite + chlorite (cps/10)	Smectite (cps/10)	Calcite (cps/10)	Carbonate (cps/10)	Pyrite (cps/10)	Clinoptilolite (cps/10)	Opal-A (cps/10)	Opal-CT (area)	Remarks
127-794A-													
1H-1, 90–92	0.90	92.5	20.5	9.0	12.0	3.0	0.0	0.0	0.0	0.0	4.0	0.0	
1H-1, 114–116	1.14	90.0	27.5	13.5	13.5	0.0	12.0	0.0	9.5	0.0	2.2	0.0	
2H-5, 87–89	13.67	104.0	18.5	8.5	9.0	1.0	0.0	0.0	3.0	0.0	1.8	0.0	
2H-5, 114–116	13.94	88.0	18.5	13.5	10.5	2.0	0.0	0.0	11.0	0.0	3.0	0.0	
3H-6, 16–18	23.96	55.5	13.5	6.0	7.0	3.0	0.0	0.0	9.0	0.0	4.0	0.0	
3H-6, 19–21	23.99	84.0	20.5	8.5	8.0	1.0	0.0	0.0	6.5	0.0	3.0	0.0	
4H-6, 103–105	4.33	109.0	21.0	9.5	9.0	0.0	0.0	0.0	1.0	0.0	3.5	0.0	
4H-6, 107–109	34.36	73.0	15.0	7.0	8.0	2.0	0.0	0.0	5.0	0.0	3.0	0.0	
5H-6, 45–47	43.25	87.0	20.5	8.0	8.5	1.5	0.0	0.0	5.5	0.0	2.2	0.0	
5H-6, 48–50	43.28	78.0	17.0	9.5	6.0	1.0	0.0	0.0	10.0	0.0	2.8	0.0	
6H-5, 102–104	51.82	83.5	28.0	6.5	5.5	1.5	0.0	0.0	2.5	0.0	3.8	0.0	
6H-5, 104–106	51.84	116.0	26.0	14.0	15.0	0.0	0.0	4.5	3.0	0.0	2.0	0.0	
7H-6, 2–4	61.82	104.5	21.5	13.5	12.5	1.0	0.0	0.0	0.0	0.0	2.5	0.0	
7H-6, 9–11	61.89	111.0	19.0	11.0	8.0	2.5	0.0	0.0	1.5	0.0	2.8	0.0	
8H-1, 136–138	65.15	88.0	20.5	9.5	7.5	3.0	0.0	0.0	0.0	0.0	3.0	0.0	
8H-1, 138–140	65.17	86.0	18.0	8.5	7.5	1.0	0.0	0.0	3.5	0.0	3.0	0.0	
9H-2, 115–119	75.95	106.0	18.0	10.0	9.5	3.0	0.0	0.0	0.0	0.0	2.0	0.0	
12H-3, 24–26	105.04	21.0	4.5	1.5	2.0	0.0	0.0	36.0	0.0	0.0	3.2	0.0	
12H-3, 79–81	105.59	59.0	11.5	4.5	7.5	1.5	0.0	0.0	1.0	0.0	5.0	0.0	
13H-2, 12–14	112.92	59.0	11.5	7.5	6.0	0.0	0.0	0.0	2.0	0.0	7.5	0.0	
14H-3, 18–20	122.48	86.0	14.0	8.5	10.0	4.5	5.5	0.0	0.0	0.0	3.5	0.0	
14H-6, 18–20	128.48	58.0	13.0	7.0	4.5	2.5	0.0	6.0	1.0	0.0	4.2	0.0	
15H-3, 17–19	133.47	31.0	6.0	2.0	3.0	0.0	0.0	0.0	1.0	0.0	10.8	0.0	
15H-6, 17–19	137.97	41.0	8.5	3.0	2.5	2.0	0.0	0.0	1.5	0.0	9.8	0.0	
16X-3, 18–20	142.98	49.5	13.0	3.5	3.5	0.0	0.0	0.0	1.0	0.0	9.5	0.0	
17X-3, 18–20	152.68	39.0	7.0	4.5	3.0	1.5	0.0	0.0	1.0	0.0	9.5	0.0	
17X-7, 18–20	158.68	38.5	8.5	4.5	3.5	2.0	0.0	0.0	2.0	0.0	6.8	0.0	
19X-1, 18–20	168.68	32.5	6.0	5.0	3.0	0.0	0.0	0.0	3.5	0.0	11.8	0.0	
20X-1, 18–20	178.38	42.0	7.0	3.5	3.0	0.0	0.0	0.0	3.0	0.0	8.2	0.0	
21X-1, 18–20	188.08	31.0	7.0	3.0	4.0	1.5	0.0	0.0	2.5	0.0	9.8	0.0	
22X-1, 18–20	197.68	49.0	7.5	3.5	3.0	3.0	0.0	3.5	1.5	0.0	6.2	0.0	
23X-1, 18–20	207.38	39.5	7.5	4.5	5.0	3.5	0.0	0.0	2.0	0.0	8.5	0.0	
23X-6, 18–20	214.88	27.0	5.0	3.0	5.5	0.0	0.0	0.0	2.5	0.0	11.2	0.0	
25X-2, 18–20	228.18	33.5	6.5	3.0	3.0	2.5	0.0	0.0	2.0	0.0	7.0	0.0	
26X-2, 18–20	237.88	34.0	9.0	4.0	3.5	3.0	0.0	0.0	0.0	0.0	8.0	0.0	
27X-2, 18–20	247.68	24.0	5.0	1.5	2.5	2.0	0.0	0.0	0.0	0.0	11.2	0.0	
27X-5, 18–20	252.18	28.0	4.0	2.0	1.0	1.0	2.0	0.0	12.5	0.0	8.5	0.0	
28X-2, 18–20	257.38	47.0	11.0	8.5	5.5	5.0	0.0	0.0	0.5	0.0	6.0	0.0	
29X-2, 21–23	267.11	34.0	7.0	5.0	3.5	2.5	0.0	0.0	4.5	0.0	7.8	0.0	
29X-5, 18–20	271.58	44.0	10.0	5.5	5.0	6.5	0.0	0.0	4.5	0.0	3.8	0.0	
30X-2, 18–20	276.78	39.5	7.0	5.5	4.5	4.5	0.0	2.5	0.0	0.0	5.8	0.0	
30X-5, 18–20	281.28	42.5	8.0	3.5	2.5	3.0	0.0	0.0	1.5	0.0	4.2	0.0	
31X-2, 18–20	286.28	30.0	6.5	2.0	3.5	2.0	0.0	8.5	0.0	0.0	5.2	0.0	
31X-5, 18–20	290.78	44.5	9.0	3.0	3.5	2.5	0.0	0.0	2.5	0.0	5.2	0.0	
31X-6, 18–20	292.28	45.0	11.5	5.5	7.5	7.5	0.0	0.0	3.0	0.0	4.5	0.0	
32X-1, 19–21	293.69	42.5	9.5	3.5	4.0	5.0	0.0	3.5	2.0	0.0	5.8	0.0	
32X-2, 20–22	295.20	52.0	12.0	6.5	7.5	4.5	0.0	3.0	2.0	0.0	3.8	0.0	
32X-3, 18–20	296.68	49.0	10.0	5.5	5.0	5.5	0.0	0.0	1.5	0.0	4.8	0.0	
33X-1, 17–19	303.47	41.5	9.5	4.0	2.0	0.0	0.0	0.0	4.0	0.0	0.0	35.2	
33X-3, 17–19	306.47	42.0	6.0	6.0	2.0	6.0	0.0	0.0	3.0	9.0	8.8	0.0	
33X-5, 17–19	309.47	51.0	12.0	5.0	3.5	8.0	0.0	0.0	1.5	8.5	3.5	0.0	
33X-7, 17–19	312.47	8.0	4.0	1.5	1.5	2.5	0.0	29.5	0.0	3.0	1.8	0.0	

Namely, the SiO_2 content is high in Units 2 and 4 and low in Units 1, 3, and 5, whereas most of the other elements are more abundant in Units 1, 3, and 5.

To examine the interelement relationship in more detail, the correlation between Al_2O_3 and the other elements was examined. The difference among lithologic units and the effect of the presence of carbonate and sulfide minerals on the relationship between Al_2O_3 and the other major elements were also examined (Fig. 8).

Figure 8A shows the relationship between Al_2O_3 and SiO_2. The two elements show a negative correlation, but with a large scatter. The correlation is improved ($r^2 = 0.77$) if samples with a higher carbonate content (>0.5% C) are excluded.

Figure 8B shows the relationship between Al_2O_3 and TiO_2. The two elements show a strong positive correlation ($r^2 = 0.90$) with an intercept of almost zero. In detail, the Ti/Al ratios of the Unit 1 samples are higher and more variable than the ratios of samples from the other four units. The two data points with exceptionally low Ti/Al ratios are samples from Unit 5 which contain a significant amount of smectite.

Figure 8C shows the relationship between Al_2O_3 and Fe_2O_3. They also show a positive correlation with an intercept near zero. However, the scatter of the data points is larger. Samples with a higher carbonate content (>0.5% C) tend to have larger Fe/Al values. Other groups of samples with higher Fe/Al ratios are those with a lower organic carbon to sulfur ratio. The sample with the highest Fe/Al ratio is a glauconitic claystone from Unit 4.

Figure 8D shows the relationship between Al_2O_3 and MnO. It is obvious from the figure that only the samples with a higher carbonate content (>0.5% C) contain more than 2% MnO.

Figure 8E shows the relationship between Al_2O_3 and MgO. The two elements show a positive correlation but with considerable scatter. Samples with a higher carbonate content (>0.5% C) have larger Mg/Al ratios. However, even after excluding those samples, the scatter is still significant. Samples from Unit 1 have consistently low Mg/Al ratios, samples from Units 2 and 3 have intermediate ratios, and samples from Units 4 and 5 tend to have higher ratios.

Figure 8F shows the relationship between Al_2O_3 and CaO. There is a positive correlation between the two elements with a relatively large scatter. Excluding samples with a carbonate carbon content larger than 0.2% improves the correlation, and the regression line passes close to the origin. Low-carbonate samples from Units 2 and 3 tend to have low Ca/Al ratios, whereas those samples from Units 1, 4, and 5 have a wider ranging Ca/Al ratio, which varies by a factor of 2.

Table 1 (continued).

Core, section, interval (cm)	Depth (mbsf)	Quartz (cps/10)	Plagioclase (cps/10)	Illite (cps/10)	Koalinite + chlorite (cps/10)	Smectite (cps/10)	Calcite (cps/10)	Carbonate (cps/10)	Pyrite (cps/10)	Clinoptilolite (cps/10)	Opal-A (cps/10)	Opal-CT (area)	Remarks
34X-1, 76–78	313.36	51.5	11.0	3.0	0.0	6.5	0.0	0.0	0.0	6.5	4.2	0.0	
35X-1, 75–77	322.95	53.5	10.5	4.0	2.0	8.0	0.0	0.0	2.0	5.5	3.0	0.0	
35X-3, 121–123	326.41	41.0	9.0	2.5	1.5	3.0	0.0	0.0	1.0	10.0	2.5	0.0	
35X-3, 135–137	326.55	48.0	8.5	6.0	2.0	6.0	0.0	0.0	3.0	16.5	5.2	0.0	
35X-6, 3–5	329.73	41.5	10.0	1.5	1.5	1.5	0.0	0.0	7.0	9.0	0.0	12.1	
35X-6, 27–29	329.97	51.0	9.5	2.0	1.0	4.0	0.0	0.0	4.0	14.0	0.0	8.8	
36X-1, 57–59	332.47	44.0	7.0	3.0	4.0	3.0	0.0	0.0	2.0	2.0	5.5	0.0	
36X-1, 102–104	332.92	38.0	8.5	3.0	3.0	1.0	0.0	0.0	5.0	2.5	0.0	5.5	
37X-3, 11–13	344.71	17.5	4.0	0.0	1.5	0.0	0.0	0.0	1.0	1.5	0.0	72.5	
37X-3, 79–81	345.39	40.5	7.5	1.0	1.0	0.0	0.0	0.0	2.5	1.5	0.0	26.2	
127-794B-													
2R-1, 39–41	164.39	38.0	6.5	0.0	0.0	0.0	0.0	0.0	1.5	0.0	6.0	0.0	
9R-1, 51–53	376.51	24.5	4.0	3.0	1.5	0.0	0.0	0.0	1.5	0.0	0.0	37.0	
9R-1, 51–53	376.52	26.5	4.5	0.0	0.0	0.0	0.0	0.0	2.0	0.0	0.0	54.1	
10R-1, 64–66	386.24	45.0	6.5	1.5	0.0	0.0	4.5	0.0	2.0	2.0	0.0	31.0	
11R-1, 56–58	395.76	176.5	4.0	0.0	2.5	0.0	0.0	0.0	2.0	0.0	2.8	0.0	
12R-2, 16–18	406.56	177.5	4.5	2.0	2.5	1.5	0.0	0.0	1.0	0.0	2.8	0.0	
12R-2, 22–24	406.62	173.5	4.0	2.0	2.0	0.0	0.0	0.0	1.5	0.0	2.5	0.0	
13R-2, 43–45	416.43	226.0	5.0	0.0	0.0	0.0	0.0	0.0	3.0	0.0	2.2	0.0	
14R-2, 68–70	426.38	242.5	4.0	2.0	1.0	2.0	0.0	0.0	3.0	0.0	2.2	0.0	
15R-2, 42–44	435.72	221.0	3.5	0.0	0.0	0.0	0.0	0.0	3.5	0.0	1.8	0.0	
16R-1, 23–25	443.43	169.0	4.0	2.0	2.0	0.0	0.0	0.0	3.0	0.0	2.2	0.0	
16R-3, 24–26	446.44	144.0	5.0	3.0	3.0	0.0	0.0	0.0	2.5	0.0	1.8	0.0	
17R-1, 39–41	453.29	264.0	4.0	0.0	0.0	0.0	0.0	0.0	2.5	0.0	1.0	0.0	
18R-1, 29–31	462.89	202.5	6.5	3.0	3.0	3.0	0.0	0.0	3.5	0.0	1.5	0.0	
19R-1, 32–34	472.62	173.5	6.5	0.0	0.0	0.0	0.0	0.0	1.0	0.0	2.0	0.0	
19R-2, 84–86	474.64	98.0	5.0	3.0	0.0	4.5	0.0	0.0	4.0	0.0	2.8	0.0	
20R-1, 94–96	482.94	191.5	7.0	0.0	0.0	1.5	0.0	0.0	4.0	0.0	0.8	0.0	
20R-1, 117–119	483.17	69.0	6.5	0.0	0.0	12.0	0.0	0.0	3.5	0.0	2.8	0.0	
20R-3, 38–40	485.38	51.0	5.0	1.5	0.0	1.5	0.0	66.0	2.5	0.0	1.2	0.0	
21R-1, 41–43	492.11	233.0	7.0	0.0	0.0	0.0	0.0	0.0	3.0	0.0	1.0	0.0	
24R-1, 54–56	521.14	55.5	9.0	0.0	0.0	0.0	0.0	20.5	2.0	0.0	2.2	0.0	
24R-5, 145–147	528.05	34.0	7.0	2.5	2.0	24.0	0.0	0.0	4.5	0.0	2.5	0.0	
26R-1, 42–44	540.42	245.5	6.0	4.0	5.5	0.0	0.0	0.0	4.0	0.0	1.5	0.0	
127-794C-													
26R-2, 88–90	644.26	238.0	0.0	3.5	2.0	2.0	0.0	0.0	2.0	0.0	0.2	0.0	
127-795A-													
2H-2, 83–85	11.63	85.5	17.0	7.0	7.0	4.5	0.0	0.0	3.5	0.0	3.8	0.0	
2H-3, 38–40	12.68	44.5	8.0	2.5	4.5	4.0	0.0	0.0	3.5	0.0	8.0	0.0	
2H-5, 81–83	16.11	103.5	19.0	7.0	8.5	2.5	0.0	0.0	0.0	0.0	2.0	0.0	
3H-1, 89–91	19.69	73.5	17.0	3.0	3.0	7.0	0.0	0.0	1.0	0.0	3.8	0.0	
3H-2, 62–64	20.92	91.5	18.5	9.0	8.5	3.0	4.0	0.0	10.5	0.0	1.8	0.0	
3H-3, 15–17	21.95	103.0	17.5	9.5	8.5	1.5	0.0	0.0	2.0	0.0	2.8	0.0	
4H-1, 115–117	9.45	79.0	21.5	10.5	9.0	5.0	0.0	0.0	10.0	0.0	2.2	0.0	Jarosite
4H-2, 113–115	30.93	105.5	22.0	10.5	7.5	1.5	0.0	0.0	0.5	0.0	2.8	0.0	
5H-3, 107–109	41.87	52.5	13.5	3.0	3.5	4.0	0.0	0.0	4.5	0.0	4.0	0.0	Gypsum, jarosite
5H-4, 89–91	43.19	104.5	22.0	8.0	9.0	5.0	3.5	0.0	2.0	0.0	2.5	0.0	
5H-6, 97–99	46.27	61.5	17.5	4.0	4.5	5.5	0.0	0.0	2.5	0.0	3.8	0.0	

Figure 8G shows the relationship between Al_2O_3 and Na_2O. The two elements show a positive correlation with an intercept near zero but with a relatively large scatter. Samples from Units 2 and 4 tend to have larger Na/Al ratios, but the ratio varies significantly within every unit.

Figure 8H shows the correlation between Al_2O_3 and K_2O. The two elements show a clear positive correlation ($r^2 = 0.81$) with an intercept near zero, which suggests that the K/Al ratio is roughly constant for most of the samples. Exceptions are the few samples from Units 4 and 5 that show a ratio as much as 2 times higher in comparison with the other samples. The sample with an exceptionally low K/Al ratio is from the base of Unit 5, and it contains a significant amount of smectite.

Figure 8I shows the relationship between Al_2O_3 and P_2O_5. The two elements show a positive correlation, but with a large scatter. When samples with higher carbonate contents are excluded, the correlation improves and the regression line passes close to the origin. For samples with lower carbonate contents, those with a higher organic carbon content tend to have slightly higher P/Al ratios.

Interpretation of the Results

Detrital Components

The result of mineral composition analysis shows that quartz (above the opal-CT/quartz boundary), plagioclase, illite, and kaolinite plus chlorite show a positive correlation with one another with nearly constant ratios, although slight differences in the ratio of quartz (or plagioclase) to illite (or kaolinite plus chlorite) are apparently present among the sites. These minerals also show a strong positive correlation with the Al_2O_3 content, supporting the conclusion that they are of detrital origin. Smear slide observation of the sediments above the opal-A/opal-CT boundary suggests that quartz and plagioclase are present dominantly as silt-size detrital grains, whereas clay minerals are present as clay-size grains. Such grain-size dependence of the detrital mineral species may explain the slight difference in their ratio among the sites.

Table 1 (continued).

Core, section, interval (cm)	Depth (mbsf)	Quartz (cps/10)	Plagioclase (cps/10)	Illite (cps/10)	Koalinite + chlorite (cps/10)	Smectite (cps/10)	Calcite (cps/10)	Carbonate (cps/10)	Pyrite (cps/10)	Clinoptilolite (cps/10)	Opal-A (cps/10)	Opal-CT (area)	Remarks
6H-2, 81–83	49.61	57.5	11.5	3.5	5.0	4.5	0.0	0.0	4.0	0.0	5.5	0.0	Gypsum, jarosite
6H-3, 89–91	51.19	102.0	21.0	10.5	9.0	2.0	0.0	0.0	3.0	0.0	2.2	0.0	
7H-5, 108–110	3.88	43.0	9.5	2.0	3.0	2.0	0.0	0.0	4.5	0.0	7.0	0.0	Jarosite
7H-5, 116–118	63.96	51.0	7.5	3.0	3.5	3.0	0.0	0.0	2.5	0.0	2.8	0.0	Jarosite
8H-4, 32–34	71.12	78.5	16.5	10.0	7.5	4.5	0.0	0.0	0.0	0.0	3.0	0.0	
8H-4, 36–38	71.16	93.5	18.0	8.0	9.5	5.0	0.0	0.0	2.0	0.0	3.0	0.0	
9H-3, 21–23	79.01	56.5	14.5	3.0	3.5	10.0	0.0	0.0	2.0	0.0	1.8	0.0	
9H-3, 45–47	79.25	101.5	19.5	7.0	7.5	4.5	0.0	0.0	0.0	0.0	2.8	0.0	
10H-1, 49–51	85.79	68.5	16.0	6.0	4.0	7.5	0.0	0.0	0.0	0.0	2.5	0.0	
11H-7, 0–2	103.80	59.0	13.0	3.0	4.5	5.5	0.0	0.0	1.5	0.0	4.0	0.0	Jarosite
11H-7, 9–11	103.89	82.0	20.0	5.5	5.5	6.5	0.0	0.0	2.0	0.0	3.5	0.0	
12H-4, 5–7	108.85	69.5	18.5	4.5	5.5	4.5	0.0	0.0	1.0	0.0	5.2	0.0	
12H-4, 10–12	108.90	77.5	19.5	8.0	5.0	5.5	0.0	0.0	3.0	0.0	3.5	0.0	
12H-4, 93–95	109.73	89.0	20.5	9.0	8.0	5.0	0.0	0.0	3.0	0.0	4.8	0.0	
12H-4, 96–98	109.76	64.5	14.5	3.0	4.5	2.0	0.0	0.0	0.0	0.0	4.5	0.0	
13H-4, 77–79	119.07	69.0	15.0	5.0	5.0	3.5	0.0	0.0	0.0	0.0	3.2	0.0	
13H-4, 96–98	119.26	66.0	14.0	5.5	6.0	4.0	0.0	0.0	3.5	0.0	4.8	0.0	
14H-4, 102–104	128.82	54.0	15.5	3.5	4.0	4.0	0.0	0.0	2.0	0.0	6.2	0.0	
14H-5, 105–107	130.35	44.0	12.5	2.5	3.0	3.0	0.0	0.0	5.5	0.0	5.2	0.0	
15H-4, 96–98	138.26	56.0	13.0	3.0	1.5	5.0	0.0	0.0	1.5	0.0	7.0	0.0	
15H-5, 36–38	139.16	33.0	7.0	0.0	1.0	0.0	0.0	0.0	2.5	0.0	11.2	0.0	Jarosite
16H-4, 95–97	147.75	55.0	12.5	3.0	3.5	2.5	2.0	0.0	1.5	0.0	6.5	0.0	
16H-1, 95–97	143.25	49.0	9.5	1.5	1.5	4.5	0.0	0.0	0.0	0.0	7.5	0.0	
18H-1, 139–141	154.29	51.0	13.0	5.5	4.5	3.0	0.0	0.0	0.0	0.0	6.5	0.0	
18H-5, 94–96	159.84	60.0	13.5	3.0	4.0	5.5	0.0	0.0	1.5	0.0	6.0	0.0	
19H-5, 94–96	169.34	70.5	17.5	4.5	4.5	4.5	0.0	0.0	1.5	0.0	4.5	0.0	
19H-7, 9–11	171.49	57.5	16.5	2.5	3.5	4.0	0.0	0.0	1.0	0.0	6.0	0.0	
21X-5, 95–97	188.55	50.0	9.0	4.0	3.5	3.0	0.0	0.0	1.5	0.0	8.8	0.0	
21X-7, 10–12	190.70	59.5	13.0	3.5	2.5	3.0	0.0	0.0	0.0	0.0	7.0	0.0	
31X-2, 109–111	281.69	55.0	15.0	4.0	4.0	5.5	0.0	0.0	1.5	0.0	7.5	0.0	
31X-5, 109–111	286.19	69.0	15.5	4.0	3.0	2.0	0.0	0.0	0.0	0.0	5.5	0.0	Jarosite
34X-1, 95–97	308.85	56.5	15.5	5.0	4.0	2.0	0.0	0.0	1.0	0.0	7.0	0.0	Jarosite?
34X-4, 95–97	313.35	71.0	18.0	3.5	3.0	0.0	0.0	0.0	1.5	0.0	6.2	0.0	Jarosite?
34X-7, 43–45	317.33	37.5	13.0	0.0	0.0	0.0	0.0	0.0	2.5	0.0	7.2	0.0	Jarosite
35X-1, 31–32	317.91	48.0	13.0	3.5	1.5	3.0	0.0	0.0	1.0	0.0	7.5	0.0	Jarosite?
35X-5, 90–92	324.50	48.5	11.0	4.0	3.5	3.0	0.0	0.0	1.0	0.0	9.2	0.0	
35X-5, 140–142	325.00	62.0	16.0	3.0	3.0	3.5	0.0	3.0	0.5	0.0	7.8	0.0	
35X-6, 9–11	325.19	29.5	5.5	0.0	0.0	1.0	0.0	0.0	1.5	0.0	0.0	72.1	
35X-6, 42–44	325.52	62.5	14.5	2.5	3.5	2.5	0.0	0.0	0.0	0.0	6.2	0.0	Jarosite
36X-1, 0–3	327.20	51.0	8.0	1.0	2.0	0.0	0.0	0.0	2.0	0.0	0.0	61.2	
36X-CC, 24–26	327.66	45.0	7.0	0.0	0.0	0.0	0.0	0.0	3.0	0.0	0.0	70.6	
37X-1, 52–54	337.42	65.5	14.0	2.0	3.0	3.0	0.0	0.0	0.0	2.5	0.0	29.9	Jarosite?
37X-1, 117–119	338.07	81.0	17.5	4.0	4.0	4.0	0.0	0.0	2.0	4.0	0.0	12.0	
127-795B-													
4R-1, 125–127	395.65	46.5	9.5	4.0	3.5	3.0	0.0	0.0	0.5	3.0	0.0	35.1	
4R-1, 125–127	395.65	42.0	10.5	2.0	0.0	3.5	6.5	0.0	1.5	11.5	0.0	32.0	
4R-2, 2–4	395.92	38.5	10.0	2.0	0.0	1.0	0.0	3.0	2.0	0.0	0.0	49.5	
5R-1, 40–42	404.50	9.5	11.0	0.0	0.0	50.0	0.0	0.0	1.5	3.0	3.0	0.0	
5R-1, 64–66	404.74	57.0	15.0	5.5	4.0	5.5	0.0	0.0	1.0	0.0	0.0	17.6	
5R-1, 71–73	404.81	55.5	3.0	1.0	1.5	0.0	0.0	0.0	1.0	0.0	0.0	79.5	
6R-1, 57–59	414.37	34.5	7.5	1.5	0.0	0.0	0.0	0.0	1.5	0.0	0.0	61.6	
6R-1, 74–76	414.54	63.0	12.0	3.5	2.0	10.0	0.0	0.0	2.5	4.5	0.0	3.6	Jarosite

Smectite, on the other hand, does not correlate with these minerals. The absence of a correlation between the smectite peak height and that of the other detrital minerals and Al_2O_3 can be attributed partly to the limitation of our method to quantify its amount. But it is likely that smectite in the sediments is dominantly of diagenetic origin, because smectite is known to be a diagenetic product of unstable materials such as volcanic glass (Inoue et al., 1978), and the input of such unstable materials to the sediments is expected, considering the many intercalations of tuff layers in certain stratigraphic intervals. We need a more detailed mineralogical and petrographical observation to confirm its origin.

The results of chemical composition analysis show that major elements other than SiO_2 and MnO are positively correlated with Al_2O_3 in samples with a low carbonate content. Among these elements, Ti is concentrated relative to Al in samples from Unit 1 and, to a lesser extent, Unit 4 (Fig. 9A). Detrital minerals such as quartz, plagioclase, smectite, and kaolinite plus chlorite are also more concentrated relative to Al in Unit 1.

Sediments of Unit 1, which is of late Pliocene to Pleistocene age, were deposited under the strong influence of glacial-interglacial climatic cycles. A significant input of eolian dust from the Asian continent is expected in these sediments, especially because the Japan Sea is located at the eastern margin of the Asian continent (Rea et al., 1985; Tsunogai et al., 1985). The dust concentration measurement in the air by Tsunogai et al. (1985) suggests a present eolian accumulation rate of approximately 5 mg/cm^2/yr in Japan, which is comparable to the bulk-accumulation rate of 3.2 to 4.6 mg/cm^2/yr estimated for upper Pleistocene sediments at Sites 794, 795, and 797 (Tamaki, Pisciotto, Allan, et al., 1990). In addition, the mineral composition of modern eolian dust in Japan is characterized by the assemblage of quartz, plagioclase, illite, and kaolinite (Inoue and Naruse, 1987), which is similar to that of the Quaternary sediments from the Japan Sea. Further, the oxygen isotopic composition of quartz from the Japan Sea Quaternary sediments supports its eolian origin (Mizota and Matsuhisa, 1985). Thus, it is likely that the detrital minerals, such as quartz, plagioclase, illite, and kaolinite plus chlorite, in the sediments from the Japan Sea are dominantly of eolian origin.

Because the Ti/Al ratio is also high in the sediments of Unit 1, it can be somehow related to the eolian input. However, the presence of probable eolian minerals, such as quartz, plagioclase, illite, and

Table 1 (continued).

Core, section, interval (cm)	Depth (mbsf)	Quartz (cps/10)	Plagioclase (cps/10)	Illite (cps/10)	Koalinite + chlorite (cps/10)	Smectite (cps/10)	Calcite (cps/10)	Carbonate (cps/10)	Pyrite (cps/10)	Clinoptilolite (cps/10)	Opal-A (cps/10)	Opal-CT (area)	Remarks
7R-1, 20–22	423.30	61.5	12.0	2.5	3.0	2.5	0.0	0.0	0.0	0.0	0.0	33.6	
7R-1, 54–56	423.64	67.0	15.0	4.5	3.5	8.5	0.0	0.0	1.5	3.0	0.0	5.5	
8R-1, 56–58	433.36	63.0	11.0	2.0	1.0	3.0	0.0	0.0	0.0	0.0	0.0	24.5	
8R-1, 107–109	433.87	32.0	7.5	1.5	1.5	1.5	0.0	0.0	2.5	0.0	0.0	57.0	
9R-2, 73–75	444.63	46.0	8.0	2.0	0.0	3.0	0.0	0.0	1.5	0.0	0.0	43.2	
9R-2, 83–85	444.73	75.5	12.0	4.0	4.0	6.0	0.0	0.0	1.0	0.0	0.0	8.4	
9R-2, 96–98	444.86	62.0	10.5	2.5	3.5	2.0	0.0	0.0	1.5	0.0	0.0	32.4	
9R-2, 103–105	444.93	66.0	10.5	3.0	2.0	5.0	0.0	0.0	0.0	0.0	0.0	26.4	
9R-2, 103–105	445.05	28.5	5.0	2.0	2.0	0.0	0.0	0.0	0.0	0.0	0.0	102.3	
10R-5, 60–62	458.60	77.0	10.5	4.5	3.0	3.5	0.0	0.0	1.5	0.0	0.0	12.6	
10R-2, 60–62	454.10	33.0	8.0	1.5	0.0	0.0	0.0	0.0	2.0	0.0	0.0	60.0	
11R-2, 61–63	463.81	50.0	9.0	4.0	3.5	2.0	0.0	0.0	1.5	3.0	0.0	31.1	
11R-3, 140–142	466.10	65.0	11.0	2.5	1.5	1.5	0.0	0.0	1.5	0.0	0.0	24.1	
12R-2, 24–26	473.14	101.5	16.0	6.5	5.5	0.0	0.0	0.0	1.5	0.0	2.5	0.0	
12R-3, 148–150	475.88	87.0	11.5	7.0	4.5	0.0	0.0	0.0	1.5	15.5	3.0	0.0	Jarosite
13R-1, 120–122	482.20	113.5	15.0	5.0	3.0	3.0	0.0	0.0	1.5	0.0	2.8	0.0	Gypsum
13R-2, 27–29	482.77	128.0	11.0	6.0	0.0	0.0	0.0	0.0	0.0	0.0	2.2	0.0	
14R-1, 115–117	491.85	97.5	10.5	3.5	0.0	3.5	0.0	0.0	1.5	0.0	2.5	0.0	Jarosite
14R-1, 123–125	491.93	97.0	11.5	4.0	0.0	4.5	0.0	0.0	3.5	0.0	3.0	0.0	Jarosite
15R-1, 84–86	500.84	118.5	10.0	6.5	3.5	4.5	0.0	0.0	0.0	0.0	3.5	0.0	
15R-2, 44–46	501.94	128.5	10.0	7.0	1.0	1.5	0.0	0.0	0.0	0.0	2.5	0.0	
16R-2, 7–9	511.27	40.0	20.5	0.0	0.0	2.5	0.0	0.0	7.5	0.0	2.0	0.0	Jarosite
16R-2, 9–11	511.29	119.5	12.0	3.0	3.5	2.5	0.0	0.0	2.0	0.0	2.8	0.0	
17R-1, 113–115	520.53	165.0	8.0	4.5	3.5	3.0	0.0	0.0	0.0	0.0	2.2	0.0	Gypsum, jarosite
17R-1, 133–135	520.73	176.5	10.5	5.5	1.5	3.0	0.0	0.0	2.0	0.0	2.8	0.0	
17R-2, 98–100	521.88	169.5	10.5	4.0	0.0	2.0	0.0	0.0	2.5	0.0	2.2	0.0	Jarosite?
18R-2, 103–105	531.63	208.5	8.0	3.0	0.0	0.0	0.0	0.0	1.0	0.0	2.0	0.0	Jarosite?
18R-2, 123–125	531.83	163.0	10.0	0.0	0.0	4.0	0.0	0.0	0.0	0.0	2.2	0.0	
19R-1, 118–119	539.88	6.0	2.0	0.0	0.0	58.5	0.0	0.0	6.5	0.0	3.2	0.0	
19R-4, 44–45	543.64	187.0	10.0	4.5	4.5	8.0	3.0	0.0	1.5	0.0	2.5	0.0	Gypsum
19R-4, 80–81	544.00	145.0	6.0	3.5	0.0	8.0	7.0	0.0	7.0	0.0	2.0	0.0	Gypsum
20R-3, 92–94	552.32	213.0	9.0	1.5	2.5	8.0	0.0	0.0	2.5	0.0	1.2	0.0	Gypsum
21R-3, 23–25	561.33	153.5	10.5	3.5	2.0	10.5	7.0	0.0	2.0	0.0	1.2	0.0	Gypsum
21R-3, 62–64	561.72	183.0	12.5	5.0	3.5	6.0	0.0	0.0	2.0	0.0	2.0	0.0	Gypsum, jarosite?
22R-1, 107–109	568.77	3.5	7.0	0.0	0.0	8.0	194.0	0.0	1.0	0.0	0.8	0.0	
22R-3, 67–69	570.81	169.5	8.0	2.5	2.0	7.5	3.5	0.0	0.0	0.0	2.2	0.0	Gypsum
22R-3, 81–83	570.95	197.5	10.5	3.5	3.0	6.0	0.0	0.0	2.0	0.0	1.2	0.0	Gypsum
22R-CC, 13–15	572.28	6.0	0.0	0.0	0.0	0.0	202.5	5.5	0.0	0.0	0.8	0.0	
23R-2, 111–113	580.01	110.5	6.0	3.0	2.5	19.0	0.0	0.0	2.5	0.0	2.5	0.0	Gypsum
23R-3, 1–3	580.41	188.0	12.0	4.5	2.0	5.0	0.0	0.0	3.0	0.0	2.0	0.0	
23R-CC, 13–15	583.35	152.0	10.0	4.0	0.0	9.5	7.5	0.0	2.0	0.0	0.8	0.0	Gypsum
24R-3, 5–6	588.99	231.0	9.5	3.0	2.0	4.0	0.0	0.0	2.5	0.0	2.0	0.0	Gypsum
24R-6, 95–97	594.39	232.0	9.0	2.5	2.5	4.0	0.0	0.0	1.5	0.0	0.0	0.0	Gypsum, jarosite
25R-4, 123–125	602.43	241.0	11.0	4.5	3.5	1.5	0.0	0.0	0.0	0.0	2.0	0.0	
25R-4, 145–146	602.65	142.5	11.0	4.0	4.0	6.0	0.0	0.0	3.0	0.0	2.0	0.0	Gypsum, jarosite?
26R-6, 75–77	614.65	296.0	11.0	3.5	4.0	2.5	0.0	0.0	1.0	0.0	1.2	0.0	Gypsum
26R-6, 78–80	614.68	197.0	11.5	4.0	3.0	3.0	0.0	0.0	3.5	0.0	1.8	0.0	Gypsum
27R-1, 72–74	616.72	204.0	10.0	3.5	3.5	1.5	0.0	0.0	4.0	0.0	2.0	0.0	Gyp, jarosite
27R-1, 75–77	616.75	225.0	9.5	3.0	3.5	3.0	0.0	0.0	2.0	0.0	1.2	0.0	Gypsum, jarosite
29R-2, 67–69	637.47	159.5	11.5	3.0	5.0	2.5	0.0	0.0	0.5	0.0	1.8	0.0	Gypsum, jarosite
29R-4, 96–98	640.76	121.5	10.5	4.5	2.5	10.0	0.0	0.0	3.0	0.0	2.2	0.0	Gypsum, jarosite
30R-1, 118–120	646.08	170.5	9.0	4.0	4.0	10.0	0.0	0.0	5.0	0.0	1.8	0.0	Gypsum, jarosite
30R-1, 148–149	646.38	148.5	11.0	4.0	4.5	6.0	0.0	0.0	3.5	0.0	2.8	0.0	Gypsum, jarosite
31R-3, 77–79	658.27	123.5	13.5	6.0	6.0	8.0	0.0	0.0	2.0	0.0	2.5	0.0	Gypsum, jarosite

kaolinite plus chlorite, is not sufficient to explain such a high observed Ti/Al ratio. We need to identify the carrier of Ti before using the Ti/Al ratio as an indicator of eolian contribution.

Contrary to Ti, Mg is enriched relative to Al in the sediments of Units 3, 4, and 5 (Fig. 9B). Smectite is also relatively abundant in Units 3 and 5. Magnesium in low-carbonate samples shows a moderate ($r^2 = 0.59$) positive correlation with the smectite peak height (Fig. 10). Because more than 10 wt% magnesium can be held in smectite (Sudo, 1974), it is possible that most of the Mg in the noncarbonate fraction is held in smectite. Because smectite is commonly formed as a diagenetic alteration product of pyroclastic material, smectite enrichment may imply a contribution of pyroclastic material to the sediments. In fact, Unit 5 at Site 794 is characterized by many intercalations of relatively thick tuff layers, which were supplied by subaqueous pyroclastic flows. Although we need to investigate further, the Mg/Al ratio can be a good indicator of the volcanic input.

Potassium is also enriched relative to Al in the sediments of Units 3 and 5 (Fig. 9C). However, it does not show any correlation with smectite peak height. The sample with the highest K/Al ratio in Unit 5 is a light-colored dolomitic-phosphatic claystone (Sample 127-794B-24R-1, 54–56 cm). Glauconitic samples also tend to have a high K/Al ratio.

Biogenic and Diagenetic Silica Components

It is well known that opal-A in pelagic and hemipelagic sediments is of biogenic origin (Heath and Moberly, 1971; Lancelot, 1973). Shipboard smear slide analysis suggests that diatom frustules are the dominant component of biogenic silica in the samples studied. It is also well known that opal-CT is transformed from opal-A and eventually transforms to quartz during burial diagenesis (Ernst and Calvert, 1969; Heath and Moberly, 1971; Murata and Nakata, 1974). Thus, opal-CT and diagenetic quartz can be regarded as originally of biogenic origin.

Sequential transformations of silica phases are observed at the four sites drilled during Leg 127. In this paper, we define the opal-A zone as the depth interval between the surface of the sediments and the shallowest occurrence of opal-CT, the opal-CT zone as the interval between the shallowest and deepest occurrence of opal-CT, and the quartz zone as below the deepest occurrence of opal-CT.

Table 1 (continued).

Core, section, interval (cm)	Depth (mbsf)	Quartz (cps/10)	Plagioclase (cps/10)	Illite (cps/10)	Koalinite + chlorite (cps/10)	Smectite (cps/10)	Calcite (cps/10)	Carbonate (cps/10)	Pyrite (cps/10)	Clinoptilolite (cps/10)	Opal-A (cps/10)	Opal-CT (area)	Remarks
32R-2, 95–97	666.65	158.5	13.0	4.0	5.0	4.5	0.0	0.0	1.0	0.0	1.8	0.0	
32R-3, 52–55	667.72	6.0	7.0	3.0	0.0	25.0	0.0	0.0	3.5	8.5	2.8	0.0	Gypsum, jarosite
32R-4, 55–57	669.25	138.5	8.5	0.0	0.0	12.5	0.0	0.0	1.0	0.0	2.0	0.0	Gypsum
32R-4, 108–110	669.78	4.0	8.5	2.0	3.0	18.5	0.0	0.0	0.0	0.0	1.0	0.0	Analcime (66)
33R-1, 124–126	675.14	268.0	10.0	2.5	4.0	1.0	0.0	0.0	0.0	0.0	0.2	0.0	Gypsum
33R-1, 131–133	675.21	111.5	10.0	1.5	2.5	11.5	0.0	0.0	0.0	10.5	1.8	0.0	
34R-1, 22–25	683.72	148.0	8.5	3.0	2.0	5.0	0.0	0.0	0.0	15.5	1.8	0.0	
127-797B-													
13H-1, 133–135	111.73	57.5	9.5	5.5	5.0	3.0	0.0	0.0	1.0	0.0	4.8	0.0	
15H-5, 61–63	136.01	67.0	13.0	9.0	9.0	3.5	0.0	0.0	1.0	0.0	3.8	0.0	
16H-4, 89–91	144.29	59.0	9.5	6.5	7.0	5.5	0.0	0.0	2.0	0.0	4.2	0.0	
16H-5, 62–64	145.52	53.0	10.5	6.5	4.5	4.0	0.0	0.0	1.0	0.0	4.5	0.0	
18H-1, 60–62	158.50	50.0	8.0	5.0	3.0	3.5	0.0	0.0	1.5	0.0	5.8	0.0	
18H-4, 60–62	163.00	20.5	4.0	2.0	2.0	1.0	0.0	22.0	1.5	0.0	5.0	0.0	
19H-2, 59–61	168.49	39.0	6.5	4.0	1.0	1.0	0.0	0.0	2.0	0.0	7.2	0.0	
20X-5, 129–131	183.19	39.5	7.0	4.5	3.0	2.0	0.0	0.0	1.5	0.0	7.5	0.0	
21X-3, 58–60	189.08	48.0	11.0	5.5	4.5	2.0	0.0	0.0	1.5	0.0	7.2	0.0	
22X-2, 61–63	197.31	40.0	9.0	3.0	2.5	1.5	0.0	0.0	0.0	0.0	9.8	0.0	
23X-5, 59–61	211.39	57.0	9.5	7.5	5.5	3.0	0.0	0.0	2.5	0.0	5.5	0.0	
24X-3, 59–61	217.89	32.5	7.0	3.0	2.5	1.5	0.0	0.0	2.5	0.0	10.0	0.0	
25X-2, 85–87	226.35	39.0	12.5	5.0	3.5	0.0	0.0	0.0	0.0	0.0	9.2	0.0	
25X-2, 139–141	226.89	50.5	9.0	3.0	2.5	1.0	0.0	0.0	1.0	0.0	6.0	0.0	
26X-4, 59–61	238.79	28.0	6.5	2.0	2.5	0.0	0.0	0.0	1.5	0.0	9.5	0.0	
27X-5, 139–141	250.79	43.0	10.5	2.5	5.0	2.0	0.0	0.0	2.0	0.0	6.0	0.0	
28X-2, 129–131	255.89	51.0	14.0	4.5	4.0	3.0	0.0	0.0	1.0	0.0	5.2	0.0	
30X-5, 16–18	278.66	64.5	10.0	6.5	3.5	2.0	0.0	0.0	2.5	0.0	3.8	0.0	Jarosite
31X-6, 63–65	290.33	47.0	11.5	6.5	5.0	4.5	0.0	0.0	1.0	0.0	4.5	0.0	Jarosite
31X-7, 20–22	291.40	55.0	11.5	2.0	3.5	4.0	0.0	0.0	1.0	0.0	4.0	0.0	
32X-4, 148–150	297.88	47.5	13.5	3.5	2.0	3.0	0.0	0.0	2.0	0.0	6.0	0.0	
32X-6, 95–97	300.35	57.5	13.0	6.5	6.0	1.0	0.0	0.0	0.0	0.0	5.2	0.0	Jarosite?
33X-2, 50–52	303.50	50.5	15.0	3.0	0.0	3.0	0.0	0.0	0.0	4.0	3.0	0.0	
33X-3, 104–106	305.54	51.0	9.5	2.0	1.0	5.0	0.0	0.0	3.5	8.0	4.0	0.0	
34X-2, 48–50	313.18	51.0	11.0	4.0	2.5	6.0	0.0	0.0	0.0	3.5	3.5	0.0	Jarosite
34X-3, 103–105	315.23	55.0	10.5	6.5	3.0	7.5	0.0	0.0	1.5	4.0	3.2	0.0	Jarosite
35X-2, 99–101	323.39	39.5	10.5	3.5	0.0	4.0	0.0	0.0	2.0	16.0	2.8	0.0	Jarosite
35X-4, 13–15	325.53	23.5	6.5	2.5	2.5	0.0	0.0	23.5	1.0	4.5	2.2	0.0	
37X-3, 140–142	344.70	48.0	13.0	3.5	3.0	5.0	0.0	0.0	0.0	8.0	4.0	0.0	
38X-1, 106–108	351.06	49.5	13.0	3.5	0.0	6.0	0.0	0.0	0.0	4.5	3.5	0.0	
38X-1, 139–141	351.39	39.5	4.0	2.0	2.0	0.0	0.0	0.0	2.5	0.0	0.0	67.2	
39X-1, 7–9	359.77	16.5	3.0	2.0	0.0	0.0	0.0	0.0	1.0	0.0	0.0	82.4	
40X-1, 53–55	369.83	51.5	9.0	5.0	2.5	8.0	0.0	0.0	3.0	6.5	0.0	0.0	
40X-2, 93–95	370.89	28.5	5.0	0.0	0.0	0.0	0.0	0.0	1.5	0.0	0.0	60.3	
42X-1, 10–12	388.00	45.5	9.5	4.0	3.0	1.0	0.0	0.0	1.0	6.0	0.0	14.7	Gypsum, jarosite
42X-CC, 13–15	388.65	24.5	5.0	2.5	0.0	0.0	0.0	0.0	2.5	7.0	0.0	54.5	Jarosite
46X-1, 43–45	427.03	35.5	6.0	2.0	0.0	0.0	0.0	0.0	1.5	4.0	0.0	53.6	
46X-1, 94–96	427.54	85.5	9.0	3.0	0.0	0.0	0.0	0.0	0.0	43.5	0.0	0.0	
47X-2, 66–68	438.36	143.5	6.0	5.0	3.5	2.5	0.0	0.0	0.0	0.0	0.0	0.0	
48X-2, 123–125	448.63	167.5	10.5	3.0	0.0	7.0	0.0	0.0	2.5	0.0	0.0	0.0	Gypsum
49X-2, 117–119	458.17	248.5	7.0	3.0	0.0	1.5	0.0	0.0	1.5	0.0	0.0	0.0	
49X-2, 124–126	458.24	138.0	8.0	5.0	0.0	3.0	0.0	0.0	2.5	0.0	0.0	0.0	
50X-1, 48–50	465.68	286.0	6.0	2.0	2.0	1.0	0.0	0.0	1.0	0.0	0.0	0.0	Gypsum, Jarosite
51X-1, 71–73	475.61	218.0	7.0	1.5	4.0	5.0	0.0	0.0	3.5	0.0	0.0	0.0	Gypsum

Opal-A and opal-CT can coexist within a stratigraphic interval in the upper part of the opal-CT zone. However, shipboard and shore-based slide observation suggests that diatom frustules (opal-A) disappear within an interval of a few meters below the shallowest occurrence of opal-CT. Similarly, the coexistence of opal-CT and diagenetic quartz is expected in the lower part of the opal-CT zone. In plotting quartz vs. plagioclase peak heights, the samples in the opal-A and opal-CT zones show similar quartz/plagioclase ratios, whereas samples from the quartz zone show higher quartz/plagioclase ratios and the two peaks tend to have a negative correlation (Fig. 11). Of the samples from the opal-CT zone, only those from the deepest part of the opal-CT zone show quartz/plagioclase ratios slightly larger than those of other samples. This fact suggests that the opal-CT to quartz transformation is also taking place within a stratigraphic interval of less than 10 m at the studied sites.

The result of chemical composition analysis shows that SiO_2 has a clearly negative correlation with Al_2O_3 (Fig. 8A). Seventeen samples from Unit 1 (opal-A zone) that contain a negligible amount of siliceous fossils based on smear slide observations and six samples from Unit 3 (opal-CT zone) that do not show a detectable opal-CT peak on XRD diagrams cluster at the lowest SiO_2 end of the plots. The linear negative correlation between Al_2O_3 and SiO_2 for low-carbonate samples together with the clustering of nonsiliceous samples at the lowest SiO_2 end suggests that the Al and Si contents of the detrital component are approximately constant and that the detrital component is diluted to various degrees by SiO_2. Strictly speaking, samples from the opal-A zone (Unit 1) have a slightly lower SiO_2/Al_2O_3 ratio, from 3.6 to 3.9 with the average value of 3.8, in comparison with samples from the opal-CT zone (Unit 3), which have an SiO_2/Al_2O_3 ratio at about 4.0. In comparison, Tada (1991b) obtained an SiO_2/Al_2O_3 ratio of 4.2 for middle Miocene siliceous sediments of northern Japan. This implies that the SiO_2/Al_2O_3 ratio of the detrital component in the sediments from the Japan Sea and its marginal areas varies slightly with time and location.

By assuming an SiO_2/Al_2O_3 ratio of 3.9 for the detrital component in all of the samples studied, it is possible to estimate the amount of silica diluting the terrigenous component (which we call excess silica) from the chemical composition data:

Table 1 (continued).

Core, section, interval (cm)	Depth (mbsf)	Quartz (cps/10)	Plagioclase (cps/10)	Illite (cps/10)	Koalinite + chlorite (cps/10)	Smectite (cps/10)	Calcite (cps/10)	Carbonate (cps/10)	Pyrite (cps/10)	Clinoptilolite (cps/10)	Opal-A (cps/10)	Opal-CT (area)	Remarks
51X-2, 81–83	477.21	273.0	7.0	4.0	2.0	1.0	0.0	0.0	1.5	0.0	0.0	0.0	Gypsum, jarosite
52X-1, 18–20	484.68	234.0	7.5	3.5	3.0	4.0	0.0	0.0	4.0	0.0	0.0	0.0	Gypsum
53X-1, 8–10	494.28	8.5	5.0	0.0	0.0	0.0	0.0	163.0	0.0	0.0	0.0	0.0	
127-797B-													
2R-2, 8–10	496.07	17.5	6.0	0.0	0.0	18.5	0.0	0.0	5.5	0.0	0.0	0.0	
2R-2, 107–109	496.47	87.0	10.0	3.0	2.5	9.5	0.0	0.0	4.0	0.0	0.0	0.0	
3R-1, 93–95	503.93	131.0	11.0	4.0	0.0	3.0	6.5	0.0	2.5	0.0	0.0	0.0	
5R-1, 112–114	523.12	89.5	11.0	4.0	1.0	6.5	0.0	0.0	4.0	0.0	0.0	0.0	Gypsum
6R-1, 108–110	532.68	162.0	7.0	2.5	1.5	6.0	0.0	0.0	1.0	0.0	0.0	0.0	Gypsum
8R-1, 103–105	551.93	61.0	6.0	1.0	2.5	4.0	0.0	30.0	4.5	0.0	0.0	0.0	Gypsum
8R-1, 106–108	551.96	66.5	11.0	0.0	0.0	8.5	6.0	0.0	3.5	0.0	0.0	0.0	Gypsum
19R-5, 99–101	662.54	120.5	12.0	0.0	0.0	12.0	6.0	0.0	3.0	0.0	0.0	0.0	Gypsum

$$\text{excess silica (wt\%)} = SiO_2\ \text{(wt\%)} - 3.9 \times Al_2O_3\ \text{(wt\%)}. \quad (1)$$

It should be noted, however, that the assumed SiO_2/Al_2O_3 ratio for the detrital component involves uncertainty as large as ±0.3, which corresponds to as much as ±5 wt% error in the estimation of excess silica for samples with a higher Al_2O_3 content. Because biogenic and diagenetic silica consist of excess silica, it is possible to derive equations to calculate the excess silica (wt%) from the XRD peak intensities of opal-A, opal-CT, and quartz. Figure 12 shows the relationship between the amount of excess silica and peak height of opal-A, opal-CT, and quartz. The opal-A peak height shows a strong positive correlation with excess silica ($r^2 = 0.93$), with an intercept of 2.96. The positive intercept represents the background intensity at 22°. The opal-CT peak area shows a strong positive correlation with excess silica ($r^2 = 0.96$), with the regression line passing close to the origin. The quartz peak height (for samples in the quartz zone) also shows a positive correlation with excess silica with a positive intercept of 13.8. The positive intercept corresponds to the amount of quartz within the detrital component. The correlation coefficient between the quartz peak height and excess silica is not very high ($r^2 = 0.86$). This is partly because the amount of quartz within the detrital component is not constant in a strict sense, but also because the crystallinity of diagenetic quartz is poor and can vary.

Using the results shown in Figure 12,

$$\text{opal-A (wt\%)} = 5.68 \times \{\text{opal-A (cps/10)} - 2.96\}, \quad (2)$$

$$\text{opal-CT (wt\%)} = \text{opal-CT (area)} \times 0.959, \text{ and} \quad (3)$$

$$\text{diagenetic quartz (wt\%)} = \{\text{quartz (cps/10)} - 13.8\} \times 0.243. \quad (4)$$

The precision is better than ±5 wt% for opal-CT and better than ±10 wt% for opal-A and diagenetic quartz. The amount of excess silica estimated using equations (2), (3), and (4) for Sites 794, 795, and 797 is shown in the right-hand column of Figures 4, 5, and 6, respectively. As is obvious from these figures, the sediments of Units 2 and 4 are rich in biogenic silica compared with those of Units 1, 3, and 5 and the lithologic unit boundaries roughly agree with the depths where the excess silica content changes abruptly.

These figures also show that the excess silica content has large-amplitude fluctuations in certain stratigraphic intervals. The upper part of Unit 3 at Site 795 is one such example. The variation of excess silica content across one of the typical dark-light cycles of Unit 3 at Site 795 was examined (Fig. 13). The dark layers contain 41 to 76 wt% of the excess silica whereas the light layer contains 8 to 31 wt%. Burrow tubes are compacted by a factor of 1.5 to 2 within both the dark and light layers, both dark and light layers are still highly porous, and additional silica cementation is not obvious from the macroscopic appearance. Consequently, significant redistribution of silica between the dark and light layers during diagenesis is unlikely (Tada, 1991a), and the variation in excess silica content between the dark and light layers seems to reflect the original variation in biogenic silica content.

Biogenic and Diagenetic Carbonate Components

Significant amounts of biogenic and diagenetic carbonates are present in several samples, but their occurrence is rather sporadic. Calcite occurs in significant amounts mostly in Unit 1, where it is present dominantly as foraminifers and nannofossils. The XRD peak of dolomite was found from Unit 2 to Unit 5. Chemical composition analysis shows that Mn, Ca, and Mg are significantly enriched in the dolomitic samples. Some of these samples are also enriched in Fe and P. Preliminary stoichiometric calculations based on the excess amounts of these elements relative to that in low-carbonate samples suggest that the dolomite may contain approximately 20 to 75 mol% Mn. Thus, some of the dolomite could be calcian rhodochrosite. Matusmoto (this volume) also reported the occurrence of rhodochrosite at Sites 794, 795, 797, and 799.

Diagenetic Sulfide Components

Pyrite is by far the dominant sulfide mineral found in the sediments studied. Berner and Raiswell (1983) suggested that sulfur is present mostly as pyrite in marine sediments although iron monosulfide may be present in the very early stages of diagenesis. Figure 14A shows the relationship between total sulfur and pyrite peak height for the samples from Site 794. As is obvious from the figure, there is a clear positive correlation between the two, supporting the statement by Berner and Raiswell.

Total sulfur, which represents the amount of pyrite, shows a positive correlation with organic carbon but with a considerably large scatter (Fig. 14B). Berner and Raiswell (1983) proposed that the organic carbon to sulfur (C/S) ratio in fine-grained marine sediments can be used as an indicator of the paleo-bottom-water oxygenation level. They also showed that the C/S ratio of modern normal marine sediments is more or less constant at a value of approximately 3. This is because the amount of reactive organic matter, which they believed roughly proportional to the amount of organic carbon remaining after decomposition during early diagenesis, limits pyrite formation in the sediments. In contrast, sufficient H_2S is produced in euxinic conditions so that the dominant control on pyrite formation is the availability of reactive iron minerals, and the C/S ratio tends to be lower than in normal marine sediments, especially where organic carbon content is low (Berner, 1984). The availability of reactive iron can be the

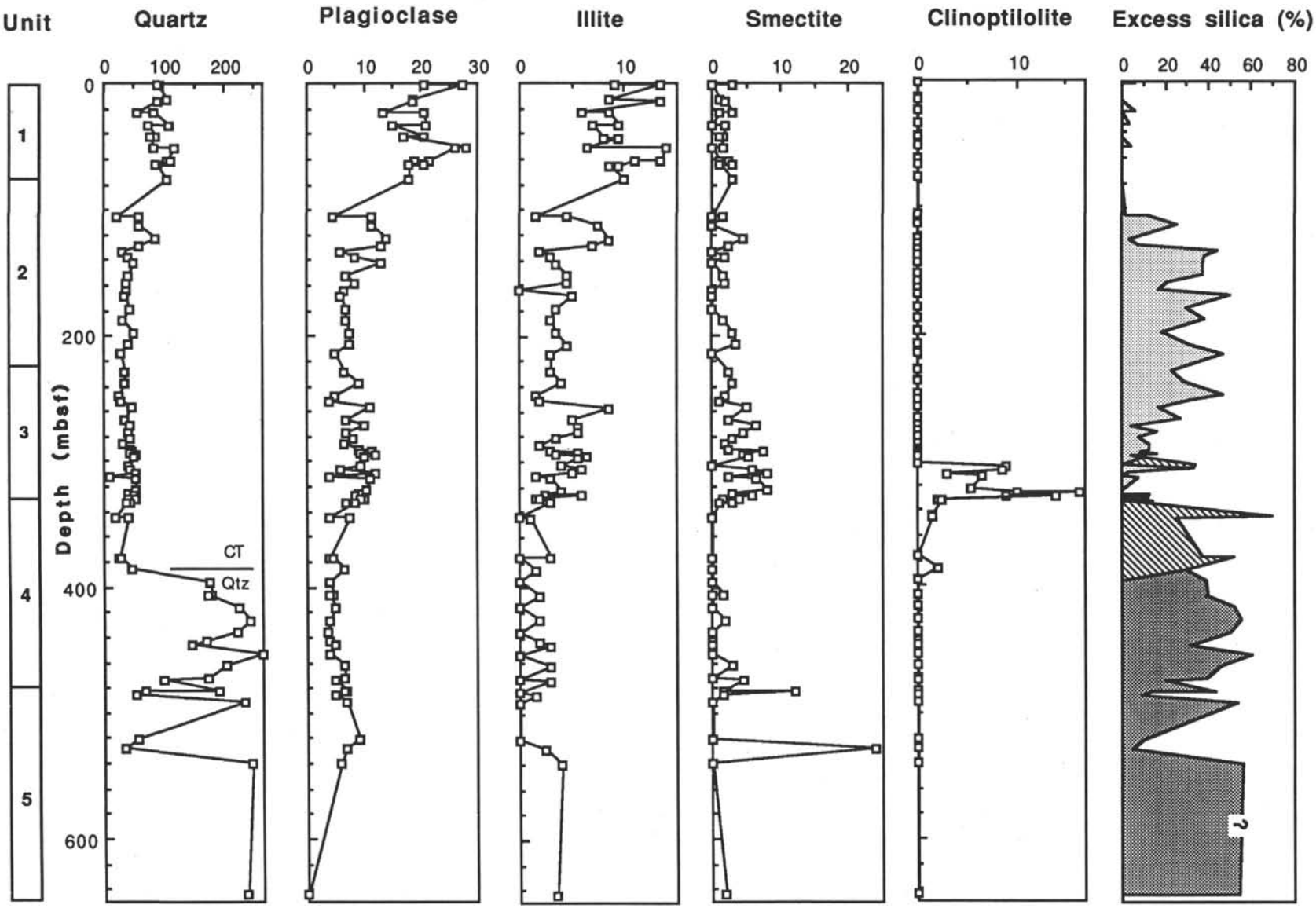

Figure 4. Vertical profiles of XRD peak intensity (cps/10) of detrital quartz, plagioclase, illite, smectite, and clinoptilolite at Site 794. Also shown is the amount of excess silica (opal-A, light shading; opal-CT, ruled; diagenetic quartz, dark shading) estimated by the method described in the text.

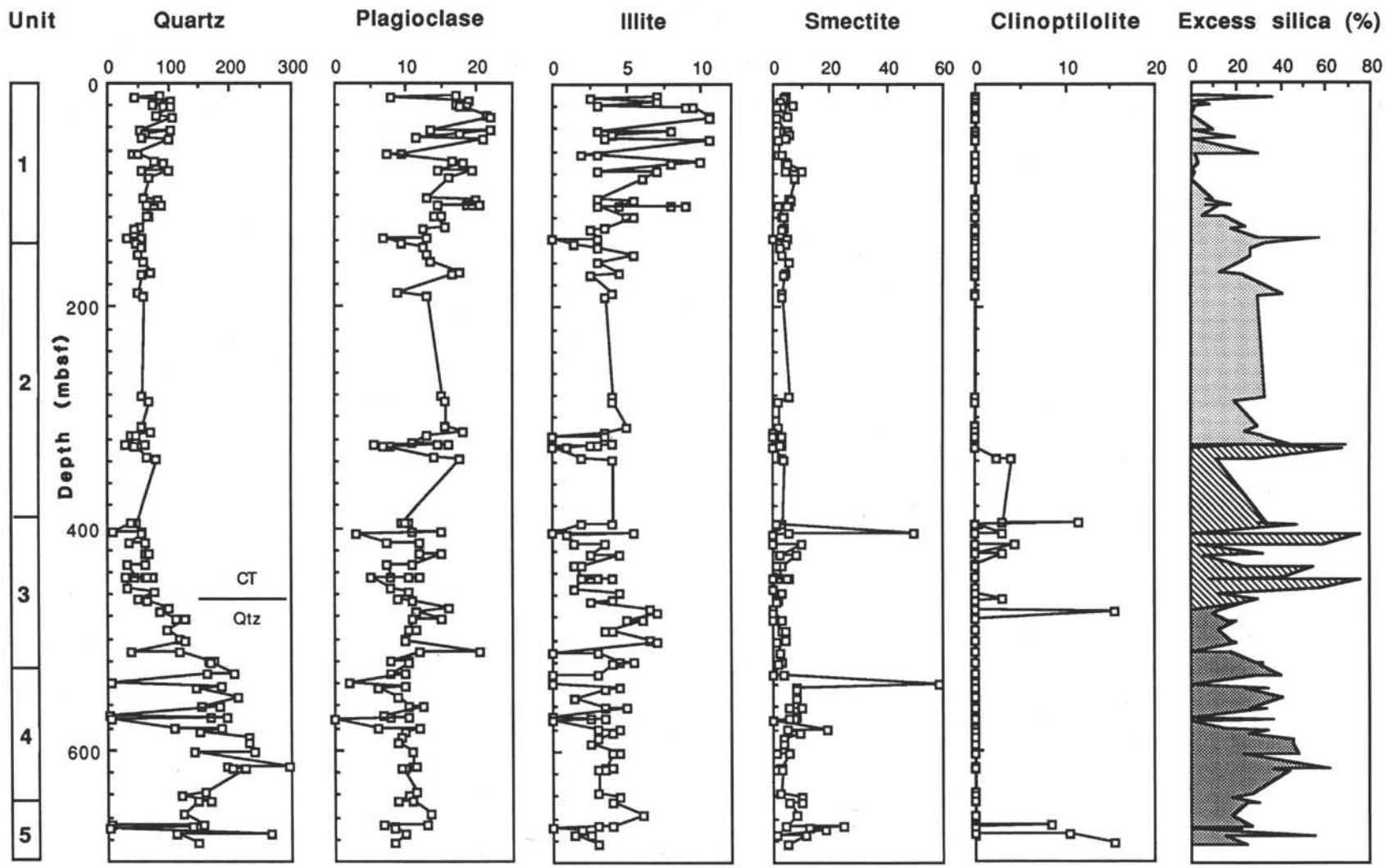

Figure 5. Vertical profiles of XRD peak intensity (cps/10) of detrital quartz, plagioclase, illite, smectite, and clinoptilolite at Site 795. Also shown is the amount of excess silica (opal-A, light shading; opal-CT, ruled; diagenetic quartz, dark shading) estimated by the method described in the text.

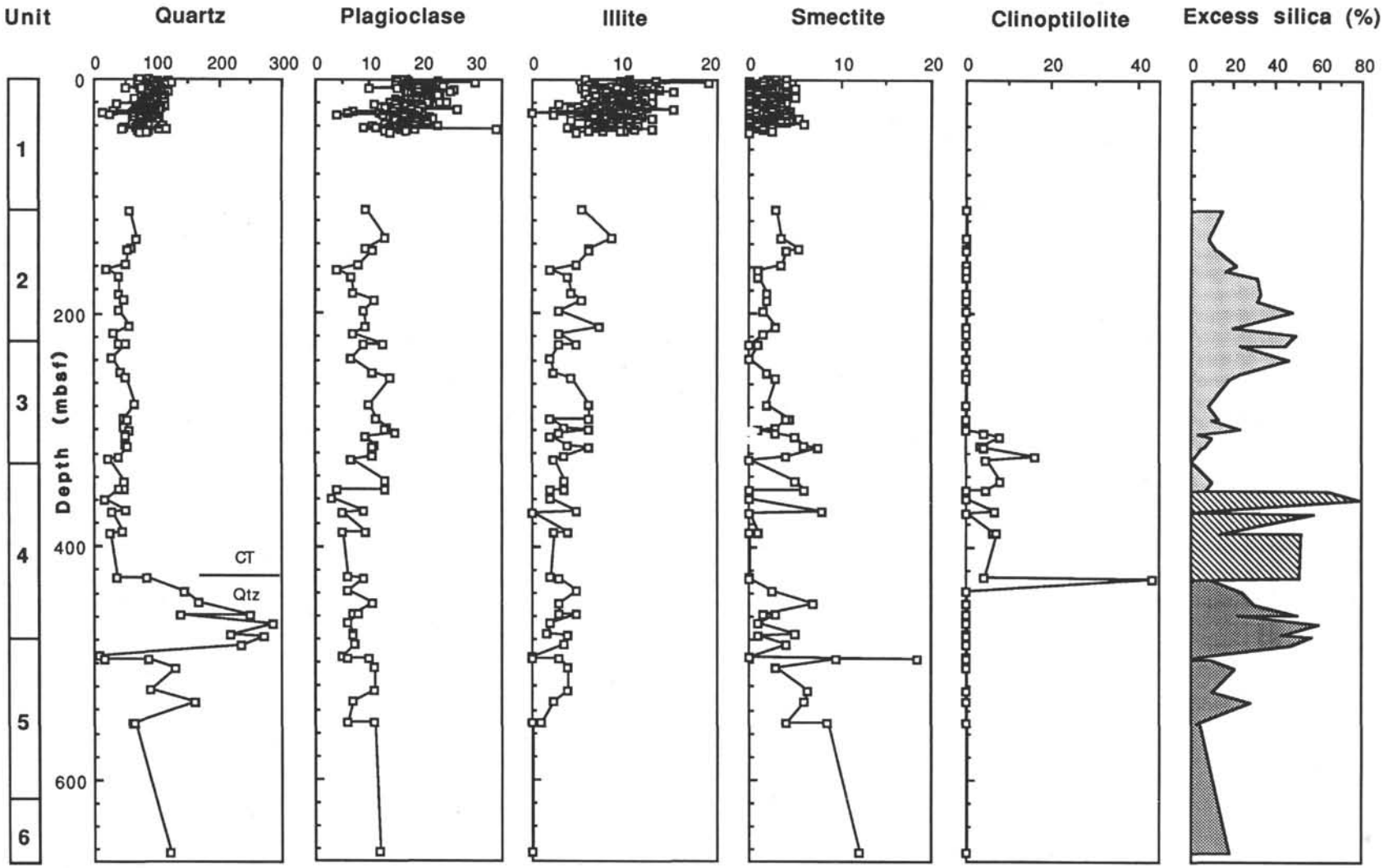

Figure 6. Vertical profiles of XRD peak intensity (cps/10) of detrital quartz, plagioclase, illite, smectite, and clinoptilolite at Site 797. Also shown is the amount of excess silica (opal-A, light shading; opal-CT, ruled; diagenetic quartz, dark shading) estimated by the method described in the text. Data for the detrital quartz, plagioclase, illite, and smectite from Quaternary sediments are from Tada et al. (this volume).

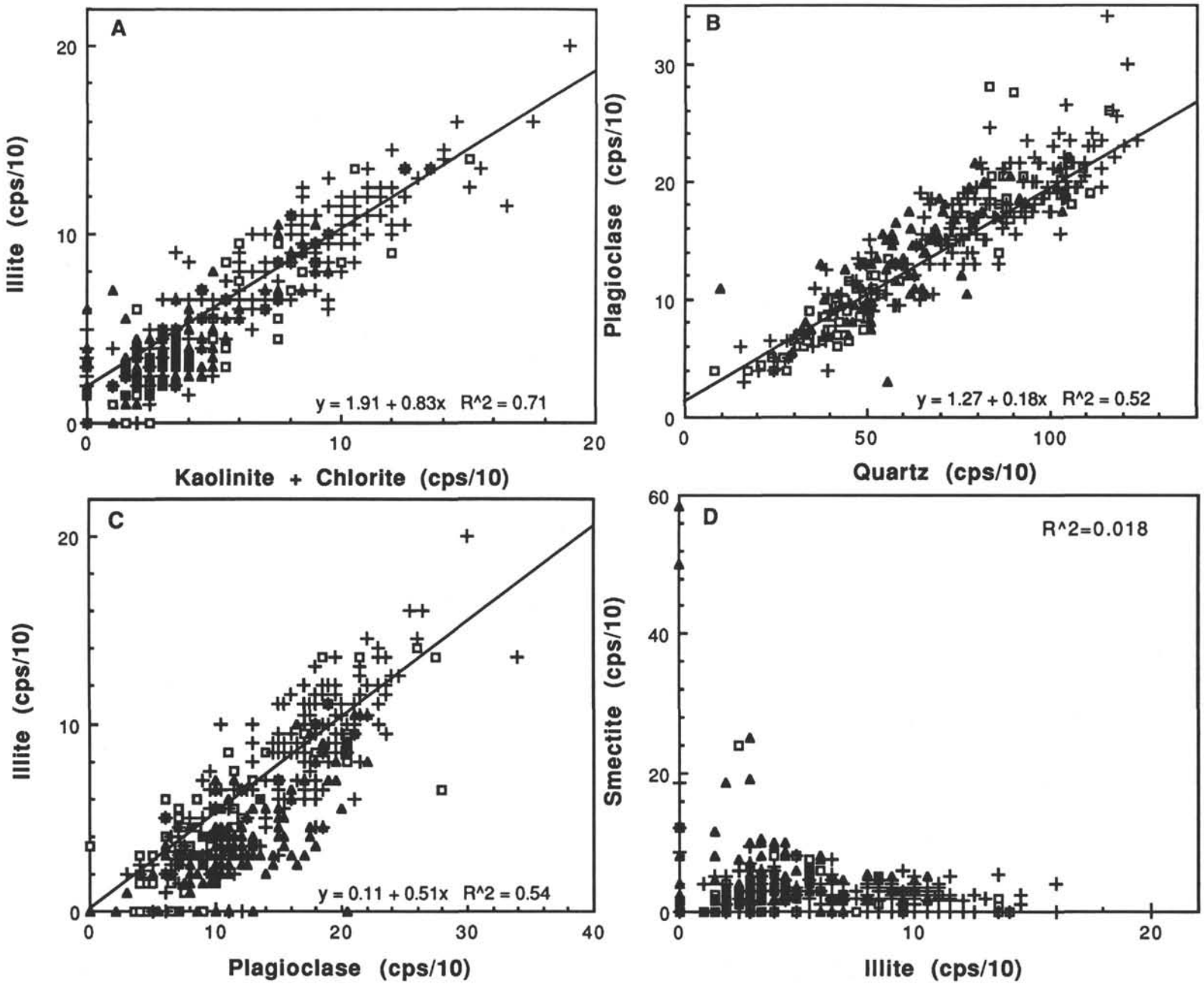

Figure 7. The relationship between the peak height of kaolinite plus chlorite and illite (**A**), detrial quartz and plagioclase (**B**), plagioclase and illite (**C**), and illite and smectite (**D**). Squares are samples from Site 797, triangles are samples from Site 795, and pluses are samples from Site 797. The data for Site 797 include Quaternary samples from Tada et al. (this volume).

Table 2. XRF, carbon, and sulfur analyses of samples from Site 794.

Core, section, interval (cm)	Depth (mbsf)	Lithology	SiO_2 (wt%)	TiO_2 (wt%)	Al_2O_3 (wt%)	Fe_2O_3[a] (wt%)	MnO (wt%)	MgO (wt%)	CaO (wt%)	Na_2O (wt%)	K_2O (wt%)	P_2O_5 (wt%)	Ignition loss (wt%)	Total (wt%)	Organic carbon (wt%)	Carbonate carbon (wt%)	Total sulfur (wt%)	Organic carbon / total sulfur
127-794A-																		
1H-1, 90–92	0.90	Light clay	56.43	0.67	15.38	6.59	0.07	2.84	1.86	2.05	2.99	0.20	10.33	99.41	0.50	0.23	0.00	
1H-1, 114–116	1.14	Dark silty clay	51.35	0.66	13.97	8.34	0.08	2.56	4.07	1.70	2.92	0.17	13.66	99.46	1.40	0.66	2.93	0.48
2H-5, 87–89	13.67	Light clay	58.67	0.75	15.27	6.84	0.06	2.68	0.72	2.24	3.46	0.13	9.15	99.96	0.21	0.00	0.03	7.00
2H-5, 114–116	13.94	Dark silty clay	53.32	0.69	14.54	9.31	0.11	2.39	1.07	3.51	3.22	0.15	10.67	98.98	1.32	0.04	3.37	0.39
3H-6, 16–18	23.96	Dark silty clay	49.12	0.56	13.35	10.09	0.07	2.08	1.07	1.61	2.56	0.39	20.06	100.95	5.24	0.16	3.65	1.44
3H-6, 19–21	23.99	Light clay	56.84	0.65	15.82	6.74	0.08	2.23	1.15	2.49	3.57	0.13	8.63	98.32	0.54	0.07	1.30	0.42
4H-6, 103–105	34.33	Light clay	57.94	0.70	14.97	5.06	0.15	2.64	1.16	1.85	3.29	0.11	10.50	98.35	0.25	0.13	0.25	1.00
4H-6, 107–109	34.36	Dark clay	52.21	0.64	13.32	7.97	0.11	2.70	0.86	1.75	3.01	0.12	16.79	99.46	1.37	0.02	0.87	1.57
5H-6, 45–47	43.25	Light clay	54.64	0.71	15.21	8.01	0.44	2.74	0.84	1.56	3.35	0.14	9.38	97.02	0.38	0.10	1.85	0.21
5H-6, 48–50	43.28	Dark clay	52.21	0.64	14.44	8.53	0.13	2.29	0.83	2.41	3.00	0.13	15.95	100.55	3.18	0.02	3.18	1.00
6H-5, 102–104	51.82	Dark clay	55.79	0.62	15.06	6.70	0.10	2.52	1.26	2.13	3.07	0.13	12.26	99.63	2.34	0.11	0.33	7.09
6H-5, 104–106	51.84	Light clay	57.76	0.78	16.01	6.49	0.14	2.96	0.97	1.66	3.56	0.12	8.77	99.21	0.33	0.15	0.12	2.75
7H-6, 2–4	61.82	Light clay	58.55	0.74	15.57	6.40	0.14	2.86	0.68	1.72	3.59	0.12	9.49	99.83	0.31	0.03	0.02	15.50
7H-6, 9–11	61.89	Dark clay	54.89	0.66	14.13	6.63	0.26	2.92	1.00	1.49	3.02	0.12	14.48	99.60	2.83	0.13	0.11	25.73
8H-1, 136–138	65.15	Dark clay	58.14	0.65	14.75	6.40	0.15	2.69	0.79	1.94	3.18	0.10	10.31	99.10	0.85	0.04	0.12	7.08
8H-1, 138–140	65.17	Light clay	54.49	0.69	14.75	6.91	0.99	2.97	0.96	1.45	3.34	0.12	12.79	99.45	2.00	0.23	0.35	5.71
9H-2, 115–119	75.95	Light clay	58.23	0.81	15.49	5.80	0.12	3.18	0.71	1.56	3.51	0.11	9.15	98.66	0.32	0.03	0.08	4.00
12H-3, 24–26	105.0	Calcareous clay	35.32	0.33	7.35	3.76	20.42	2.23	5.37	0.90	1.61	0.30	24.26	101.84	0.35	4.61	0.04	8.75
12H-3, 79–81	105.6	Diatomaceous silty clay	56.95	0.56	13.44	5.92	0.39	2.75	0.60	1.68	2.74	0.08	14.24	99.36	0.51	0.03	0.11	4.64
13H-2, 12–14	112.9	Diatomaceous silty clay	63.23	0.39	8.68	4.40	0.12	1.64	0.46	1.42	1.81	0.05	18.71	100.90	0.59	0.00	0.42	1.40
14H-3, 18–20	122.5	Silty clay	54.40	0.62	13.60	5.35	0.11	2.47	0.83	1.67	2.53	0.09	19.24	100.89	0.53	0.00	0.17	3.12
14H-6, 18–20	128.5	Diatomaceous silty clay	58.33	0.56	12.70	5.16	2.08	2.34	1.16	1.91	2.53	0.11	12.21	99.08	0.68	0.46	0.40	1.70
15H-3, 17–19	133.5	Diatom ooze	69.51	0.27	6.58	3.36	0.12	1.44	0.30	1.26	1.34	0.05	16.66	100.89	0.51	0.00	0.26	1.96
15H-6, 17–19	138.0	Diatom ooze	58.04	0.27	5.86	3.02	0.08	1.20	0.39	1.42	1.23	0.05	31.19	102.74	0.32	0.00	0.16	2.00
16X-3, 18–20	143.0	Diatom ooze	68.57	0.40	9.86	3.92	0.31	2.11	0.70	1.81	1.91	0.07	10.49	100.16	0.40	0.08	0.08	5.00
17X-3, 18–20	152.7	Diatom ooze	68.67	0.36	9.10	4.55	0.09	1.94	0.42	1.37	1.84	0.06	11.36	99.77	0.50	0.01	0.14	3.57
17X-7, 18–20	158.7	Diatomaceous clay	65.60	0.40	9.93	6.20	0.12	2.24	0.44	1.55	2.05	0.05	12.11	100.70	0.33	0.02	0.19	1.74
19X-1, 18–20	168.7	Diatom ooze	75.09	0.30	6.94	3.52	0.12	1.67	0.34	1.20	1.41	0.05	11.94	102.58	0.45	0.02	0.43	1.05
20X-1, 18–20	178.4	Diatom ooze	69.30	0.38	9.01	4.70	0.16	2.14	0.39	1.22	1.86	0.05	12.04	101.26	0.33	0.00	0.48	0.69
21X-1, 18–20	188.1	Diatom ooze	72.07	0.30	7.73	3.71	0.13	1.79	0.36	1.25	1.42	0.05	12.59	101.39	0.54	0.00	0.39	1.38
22X-1, 18–20	197.7	Diatomaceous clay	63.26	0.47	11.12	5.41	0.26	2.86	0.53	1.40	2.25	0.06	12.81	100.43	0.56	0.01	0.25	2.24
23X-1, 18–20	207.4	Diatom ooze	67.02	0.37	9.48	4.52	0.23	2.61	0.47	1.49	1.79	0.05	12.30	100.33	0.61	0.00	0.51	1.20
23X-6, 18–20	214.9	Diatom ooze	73.40	0.28	6.69	3.54	0.19	1.98	0.33	1.06	1.30	0.04	12.44	101.24	0.57	0.01	0.51	1.12
25X-2, 18–20	228.2	Diatomaceous clay	62.85	0.43	12.35	4.32	0.35	2.71	0.63	2.09	2.62	0.07	11.37	99.79	0.43	0.00	0.13	3.31
26X-2, 18–20	237.9	Diatomaceous clay	66.36	0.36	9.11	4.44	0.39	3.48	0.44	1.74	1.74	0.06	12.93	101.05	0.53	0.00	0.31	1.71
27X-2, 18–20	247.7	Diatom ooze	72.50	0.27	7.08	3.32	0.18	2.29	0.36	1.28	1.29	0.05	13.08	101.69	0.73	0.00	0.23	3.17
27X-5, 18–20	252.2	Diatom ooze	58.01	0.34	9.40	10.12	0.31	2.70	0.59	1.92	1.90	0.05	16.66	101.99	1.03	0.06	4.21	0.24
28X-2, 18–20	257.4	Diatomaceous clay	61.63	0.47	11.38	5.94	0.39	4.10	0.56	1.73	2.25	0.07	13.05	101.57	0.98	0.00	0.66	1.48
29X-2, 21–23	267.1	Diatomaceous clay	63.88	0.36	9.66	5.10	0.56	3.45	0.55	1.52	1.76	0.06	11.38	98.28	0.81	0.03	0.83	0.98
29X-5, 18–20	271.6	Diatomaceous clay	57.43	0.52	13.30	6.31	0.71	4.08	0.73	2.12	2.56	0.07	10.79	98.61	0.46	0.07	0.51	0.90
30X-2, 18–20	276.8	Diatomaceous clay	58.49	0.48	11.97	6.01	0.41	3.95	0.54	1.51	2.36	0.08	12.75	98.54	0.81	0.00	0.50	1.62
30X-5, 18–20	281.3	Diatomaceous clay	58.63	0.50	12.40	5.82	0.35	4.21	0.56	1.33	2.37	0.07	12.46	98.70	0.84	0.00	0.35	2.40
31X-2, 18–20	286.3	Diatomaceous clay	57.38	0.37	9.50	4.75	4.27	3.50	1.90	1.19	1.84	0.11	14.09	98.90	0.66	0.96	0.71	0.93
31X-5, 18–20	290.8	Dark diatomaceous clay	59.29	0.52	12.30	5.78	0.50	3.94	0.70	1.14	2.43	0.08	12.60	99.29	1.43	0.01	0.68	2.10

Table 2 (continued).

31X-6, 18–20	292.3	Diatomaceous clay	57.44	0.54	13.10	6.45	0.32	4.21	0.64	1.54	2.60	0.07	12.31	99.21	0.66	0.00	0.58	1.14
32X-1, 19–21	293.7	Light claystone	60.38	0.46	11.35	5.75	0.28	3.66	0.51	1.27	2.22	0.07	13.34	99.29	0.85	0.00	0.72	1.18
32X-2, 20–22	295.2	Dark claystone	55.10	0.53	12.08	6.02	1.41	3.98	1.10	1.11	2.66	0.09	15.03	99.11	2.08	0.26	0.91	2.29
32X-3, 18–20	296.7	Light claystone	55.75	0.56	13.63	6.58	0.49	4.37	0.69	1.31	2.89	0.07	12.58	98.93	0.98	0.01	0.66	1.48
33X-1, 17–19	303.5	Dark siliceous claystone	68.78	0.40	9.49	4.53	0.18	2.63	0.37	0.98	2.07	0.05	10.49	99.95	1.18	0.01	0.82	1.44
33X-3, 17–19	306.5	Tuffaceous siltstone	53.02	0.50	13.06	9.61	0.44	3.06	0.63	1.17	2.89	0.07	12.56	97.02	0.31	0.00	2.98	0.10
33X-5, 17–19	309.5	Light claystone	57.92	0.58	14.24	6.00	0.20	3.64	0.56	1.41	3.21	0.11	10.71	98.58	0.54	0.00	0.35	1.54
33X-7, 17–19	312.5	Calcareous claystone	19.36	0.14	3.68	3.60	19.98	4.17	14.59	0.71	0.93	0.62	33.64	101.43	1.43	6.78	0.20	7.15
34X-1, 76–78	313.4	Light claystone	57.01	0.59	15.06	5.99	0.23	3.56	0.53	1.25	3.35	0.08	11.54	99.20	0.79	0.00	0.33	2.39
35X-1, 75–77	323.0	Dark claystone	55.57	0.57	14.94	6.01	0.14	3.26	0.47	1.43	3.53	0.08	13.64	99.64	1.75	0.00	0.07	25.00
35X-3, 121–123	326.4	Dark claystone	51.93	0.50	13.05	6.15	1.76	3.43	1.28	1.24	3.11	0.10	16.97	99.53	2.81	0.42	1.09	2.58
35X-3, 135–137	326.6	Black claystone	53.44	0.48	12.47	6.20	0.23	2.92	0.61	1.37	3.22	0.10	19.87	100.90	6.17	0.00	0.76	8.12
35X-6, 3–5	329.7	Dark claystone	57.39	0.48	11.83	6.66	0.30	3.39	0.63	1.35	2.84	0.10	14.58	99.55	2.42	0.00	1.73	1.40
35X-6, 27–29	330.0	Light claystone	58.94	0.49	13.18	6.23	0.18	3.16	0.45	1.35	3.31	0.06	11.76	99.09	0.87	0.00	1.04	0.84
36X-1, 57–59	332.5	Dark claystone	55.45	0.47	12.49	6.57	0.24	5.14	0.50	1.53	2.85	0.08	13.19	98.51	1.79	0.00	0.76	2.36
36X-1, 102–104	332.9	Light claystone	54.06	0.44	11.13	6.69	0.67	4.99	1.03	1.23	2.41	0.11	17.76	100.51	4.07	0.01	1.82	2.24
37X-3, 11–13	344.7	Dark chert	83.87	0.18	4.70	1.71	0.16	1.37	0.39	0.66	0.99	0.04	6.20	100.27	0.54	0.08	0.26	2.08
37X-3, 79–81	345.4	Light claystone	69.00	0.42	10.51	4.81	0.67	3.79	0.59	1.13	2.33	0.06	8.19	101.51	0.48	0.10	0.74	0.65
127-794B-																		
2R-1, 39–41	164.4	Diatomaceous clay	64.03	0.40	9.86	5.80	0.18	2.30	0.46	2.31	2.09	0.06	13.57	101.05	0.22	0.00	0.05	4.40
9R-1, 51–53	376.5	Light porcellanite	75.67	0.26	6.93	2.90	0.15	2.05	1.23	0.98	1.47	0.06	7.66	99.35	0.69	0.20	0.64	1.08
9R-1, 51–53	376.5	Dark porcellanite	75.60	0.26	6.98	2.95	0.15	2.02	1.23	0.95	1.47	0.06	7.54	99.19	0.63	0.12	0.46	1.37
10R-1, 64–66	386.2	Light siliceous claystone	71.00	0.31	8.37	3.52	0.16	2.21	2.11	1.25	1.75	0.08	8.14	98.90	0.54	0.31	0.84	0.64
11R-1, 56–58	395.8	Gray porcellanite	77.15	0.33	7.74	2.96	0.04	1.54	0.23	1.07	1.51	0.05	6.51	99.12	0.62	0.00	0.33	1.88
12R-2, 16–18	406.6	Light siliceous claystone	77.36	0.29	8.10	2.74	0.05	1.82	0.83	1.12	1.39	0.06	7.23	100.99	0.73	0.08	0.81	0.90
12R-2, 22–24	406.6	Dark siliceous claystone	75.35	0.31	7.77	3.26	0.05	1.59	0.47	1.18	1.48	0.05	8.10	99.61	1.04	0.00	0.94	1.11
13R-2, 43–45	416.4	Light siliceous claystone	78.29	0.35	8.07	2.70	0.06	1.60	0.36	0.80	1.47	0.07	6.18	99.93	0.59	0.00	0.75	0.79
14R-2, 68–70	426.4	Light siliceous claystone	80.22	0.30	6.66	2.64	0.04	1.38	0.39	1.33	1.38	0.05	6.17	100.56	0.76	0.00	0.81	0.94
15R-2, 42–44	435.7	Light siliceous claystone	79.67	0.32	7.55	2.71	0.03	1.70	0.25	0.86	1.46	0.06	7.10	101.69	0.75	0.01	0.55	1.36
16R-1, 23–25	443.4	Dark siliceous claystone	71.02	0.32	8.32	3.46	0.07	2.36	0.28	0.87	2.00	0.08	10.45	99.24	2.13	0.01	1.10	1.94
16R-3, 24–26	446.4	Light calcareous claystone	69.85	0.37	8.82	3.85	0.08	2.97	0.29	1.20	2.09	0.07	8.92	98.51	1.17	0.02	0.88	1.33
17R-1, 39–41	453.3	Dark porcellanite	79.83	0.26	6.51	2.46	0.03	1.36	0.17	1.02	1.58	0.06	7.12	100.40	1.20	0.02	0.71	1.69
18R-1, 29–31	462.9	Gray siliceous claystone	68.99	0.38	9.85	4.14	0.07	2.71	0.27	1.23	2.60	0.07	10.24	100.54	1.08	0.01	1.00	1.08
19R-1, 32–34	472.6	Light siliceous claystone	69.35	0.37	9.89	4.33	0.34	3.47	0.79	1.04	2.77	0.08	7.68	100.13	1.36	0.17	0.90	1.51
19R-2, 84–86	474.6	Light glauconitic claystone	64.38	0.38	9.08	10.51	0.09	3.70	0.43	0.79	2.84	0.08	8.05	100.34	0.55	0.01	1.06	0.52
20R-1, 94–96	482.9	Light siliceous claystone	67.32	0.27	7.09	4.06	0.93	3.52	2.33	0.72	2.10	0.10	9.88	98.33	1.36	0.77	0.74	1.84
20R-1, 117–119	483.2	Dark claystone	56.86	0.34	11.45	6.25	0.24	6.86	0.76	1.22	2.31	0.10	11.33	97.73	1.58	0.06	0.90	1.76
20R-3, 38–40	485.4	Light calcareous claystone	31.67	0.14	3.57	3.20	6.78	6.95	18.99	0.39	1.29	0.09	29.42	102.48	0.49	6.95	0.30	1.63
21R-1, 41–43	492.1	Light claystone													0.61	0.00	0.59	1.03
24R-1, 54–56	521.1	Calcareous claystone	43.98	0.31	8.03	4.54	10.58	3.85	5.40	0.70	3.34	0.31	19.18	100.23	1.78	3.19	0.90	1.98
24R-5, 145–147	528.1	Dark claystone	52.66	0.35	13.22	7.02	0.30	7.78	1.09	2.32	1.91	0.08	11.76	98.50	0.52	0.09	0.81	0.64
26R-1, 42–44	540.4	Gray claystone													0.72	0.00	0.70	1.03
127-794C-																		
26R-2, 88–90	644.3	Light siliceous claystone													0.05	0.00	0.00	

[a] Total Fe is expressed as Fe_2O_3.

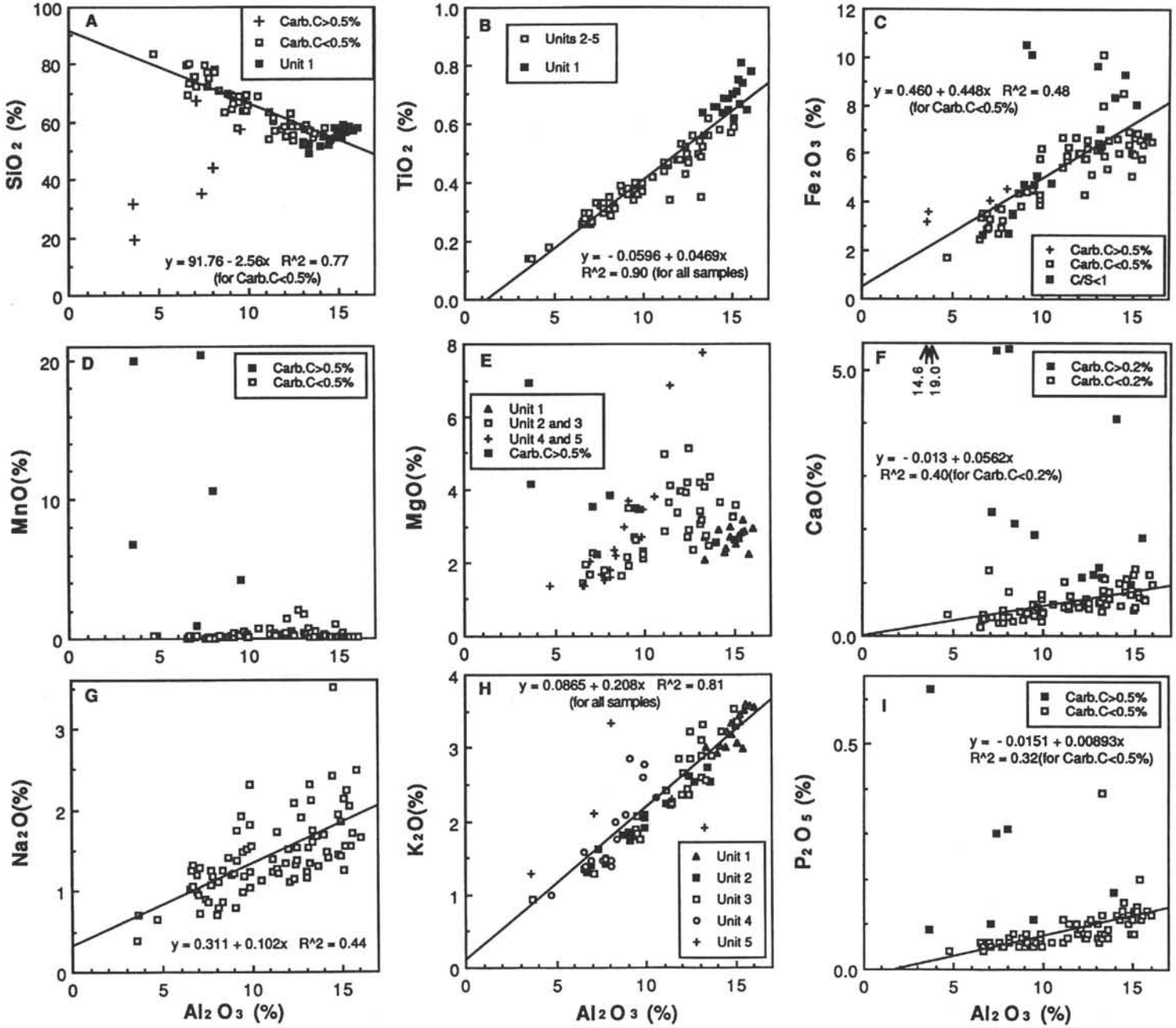

Figure 8. The relationship between the contents of Al_2O_3 and SiO_2 (**A**), TiO_2 (**B**), Fe_2O_3 (**C**), MnO (**D**), MgO (**E**), CaO (**F**), Na_2O (**G**), K_2O (**H**), and P_2O_5 (**I**) for samples from Site 794.

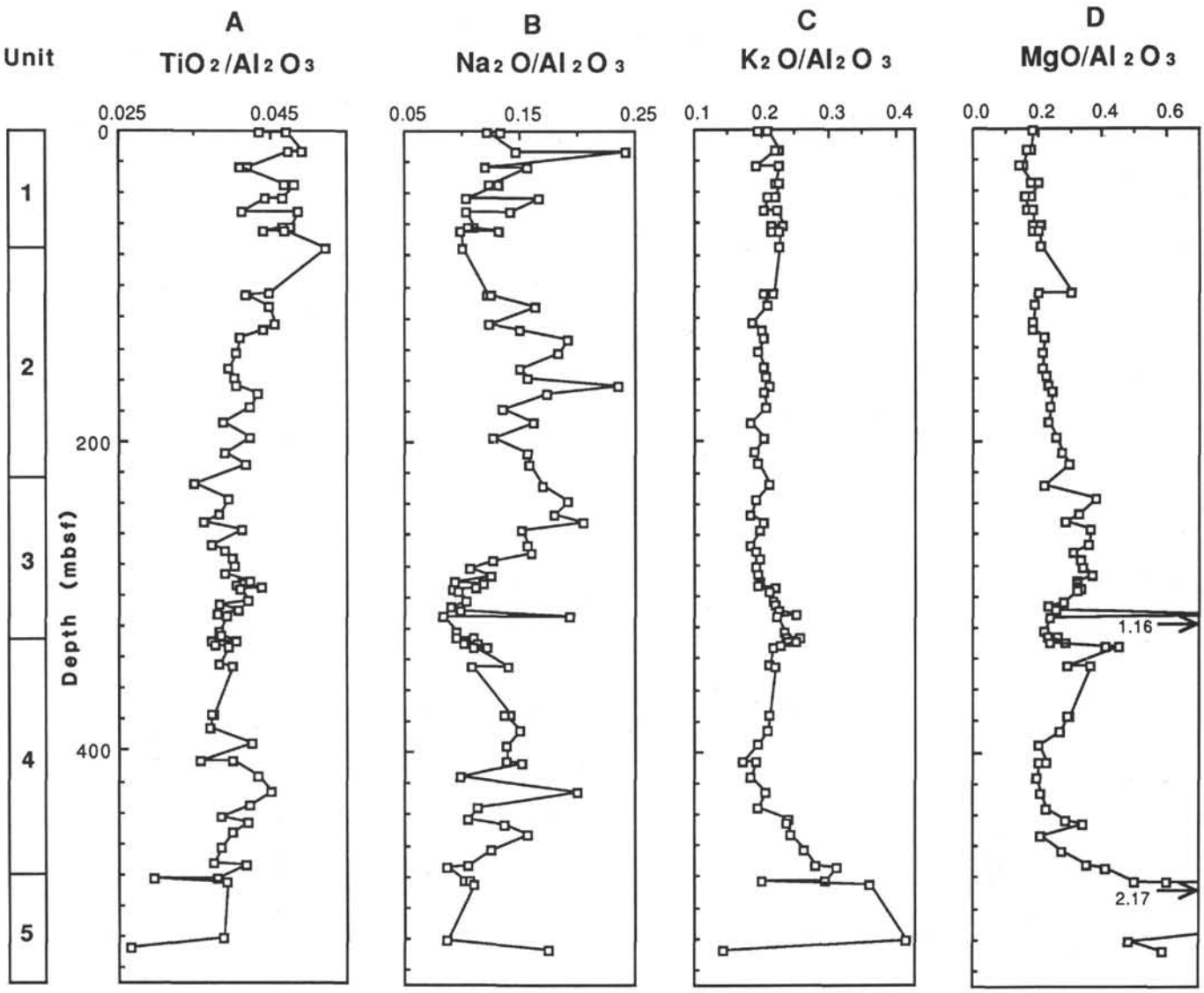

Figure 9. Vertical profiles of TiO_2/Al_2O_3 (**A**), Na_2O/Al_2O_3 (**B**), K_2O/Al_2O_3 (**C**), and MgO/Al_2O_3 (**D**) ratios for samples from Site 794.

limiting factor of pyrite formation in biogenic calcareous or siliceous sediments in which iron content is low as a result of dilution by biogenic components (Berner, 1984).

On the organic carbon vs. total sulfur diagram in Figure 14B, samples from Units 1 and 3 tend to plot above the normal marine domain of Berner and Raiswell (1983), whereas samples from Units 2, 4, and 5 plot within the normal marine domain. A few samples from Units 1 and 3 plot below the normal marine domain. The low C/S ratio of the samples from Units 1 and 3 suggests that they might have been deposited under euxinic conditions. In consideration that the dark layers of Subunit 1A are commonly laminated and that those in Unit 3 are poorly bioturbated, it is possible that they were deposited under euxinic conditions. This interpretation is also consistent with sulfur isotopic data for Site 795 Unit 1 samples presented by Masuzawa (this volume), who showed that pyrite in some of the samples from Units 1 and 3 has very light sulfur isotopic ratios close to that of seawater. On the other hand, samples from Unit 4 tend to plot within the normal marine domain, though some of them plot slightly above it. This does not seem consistent with the relatively good preservation of lamination within Unit 4, which is suggestive of oxygen-deficient bottom water. However, this apparent inconsistency can be explained by the reactive iron limitation of pyrite formation within Unit 4 sediments caused by the dilution effect by biogenic silica.

Figure 15 shows a vertical variation of organic carbon, sulfur, and C/S and S/Fe_2O_3 ratios at Site 794. As shown by the figure, the S/Fe_2O_3 ratio for samples with a low C/S ratio in Units 1 and 3 is close to 0.4, suggesting that approximately 50% of the total Fe is pyritized. Because almost all reactive iron is pyritized in euxinic conditions, this ratio perhaps represents the upper limit for pyritization. The ratio of S/Fe_2O_3 in Units 2 and 5 is generally low, suggesting that pyrite formation is not limited by reactive iron, whereas the ratio in Unit 4 is much higher and closer to 0.4, which suggests that pyrite formation can be limited by reactive iron. Figure 15 further shows that intervals with high organic carbon and those with low C/S are not exactly the same, but that high organic carbon intervals tend to start lower within Unit 1.

SUMMARY

The lithostratigraphy of the Neogene and Quaternary sediments recovered from the Japan Sea during Leg 127 was revised based on the kind and relative amount of biogenic components, sediment color,

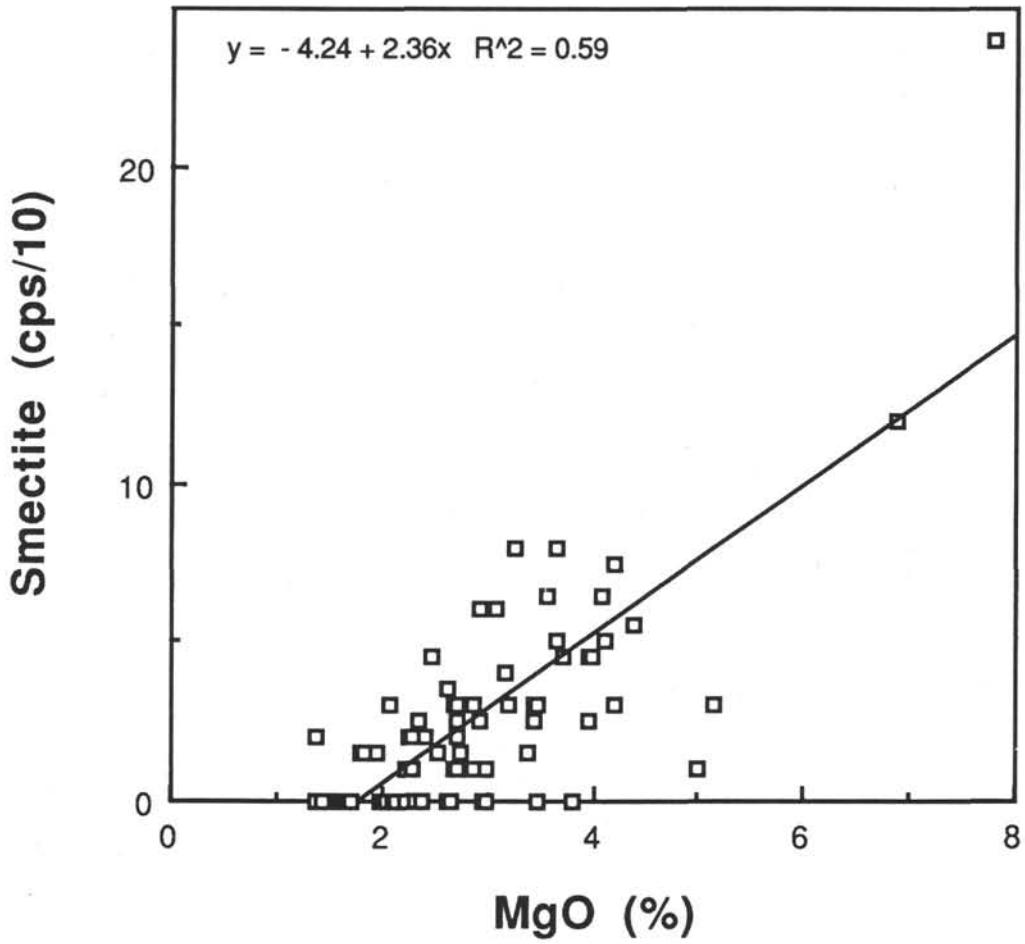

Figure 10. Relationship between MgO content and smectite peak height for samples from Site 794.

and sedimentary structures, with an emphasis on the dark-light sedimentary cycles. According to the revised lithostratigraphy, the sediments are divided into six units (labeled 1 through 6 in descending order), of which Units 1 through 5 are composed dominantly of fine-grained hemipelagic sediments.

Chemical and mineral composition analyses were conducted to quantify the amount of biogenic (and diagenetic) silica, characterize the nature of the detrital component, and examine the relation between the revised lithologic units and the pattern of compositional variation. Based on the results, Units 1 through 5 are characterized as follows.

Unit 1 is composed of silty claystone with distinct dark-light cycles. Organic matter and pyrite enrich the dark layers. The dark-light cycles may reflect fluctuation of the bottom-water oxygenation level between oxic and anoxic or even euxinic conditions based on the generally low and fluctuating C/S ratio and the sedimentary structures. The sediments are poor in biogenic silica, and the terrigenous component is characterized by a high and slightly variable Ti/Al ratio and abundant quartz, plagioclase, illite, and kaolinite plus chlorite contents, which may imply a significant contribution of eolian material.

Unit 2 is composed of heavily bioturbated diatomaceous ooze with a C/S ratio comparable to that of normal marine oxic sediments. Both the intense bioturbation and the normal C/S ratio suggest well-oxygenated bottom-water conditions. The sediments of this unit are generally poor in organic carbon and pyrite; instead they contain 20 to 60 wt% biogenic silica in amounts fluctuating on a scale of a few tens of meters.

Unit 3 is characterized by dark-light cycles of silty claystone. The dark layers are generally rich in organic matter and pyrite. The mode of bioturbation together with the relatively low and variable C/S ratio suggests a fluctuating bottom-water oxygenation level between oxic and anoxic or even euxinic conditions. Biogenic (or diagenetic) silica is relatively sparse and decreases downsection toward the bottom of Unit 3. The chemical composition of the sediments in Unit 3 tends to have higher Mg/Al and K/Al ratios; the former tends to occur in the upper part of the unit whereas the latter occurs in the basal part of Unit 3.

Unit 4 is characterized by the alternation of dark chert and light siliceous shale in Subunit 4A and parallel laminated to weakly bioturbated (mostly by horizontal burrows) siliceous claystone in Subunit 4B. Dark-light cycles in Subunit 4A are less distinct and more bioturbated compared with those in Unit 3. The C/S ratio of the sediments in this unit is generally within the range of normal marine sediments. However, this could be caused by the reactive iron limitation of pyrite formation resulting from the dilution effect of biogenic silica. The amount of diagenetic silica is relatively high, generally between 20 and 60 wt%. Glauconite pellets and carbonate micronodules and stringers were found in the lower half of Subunit 4B.

Unit 5 is composed of dark claystone with carbonate micronodules and stringers and horizontal burrows. The C/S ratio for the claystone is close to the normal marine ratio and its diagenetic silica content is generally low. Many subaqueous tuff layers as thick as 20 m are intercalated in the unit. The composition of the claystone is characterized by a high Mg/Al ratio and high smectite content, which may reflect the contribution of pyroclastic material.

The results of compositional analyses confirm that the boundaries of the revised lithologic units approximately agree with the stratigraphic levels where biogenic (or diagenetic) silica content changes drastically.

ACKNOWLEDGMENTS

This study is supported by the Grant-in-Aid for Scientific Research of the Ministry of Education, Science and Culture of Japan No. 62470045 provided to R. Tada and No. 01470053 provided to A. Iijima. We are grateful to R. Siever, C. M. Isaacs, and K. Pisciotto for reviews and suggestions.

REFERENCES

Berner, R. A., 1984. Sedimentary pyrite formation: an update. *Geochim. Cosmochim. Acta,* 48:605–615.

Berner, R. A., and Raiswell, R., 1983. Burial of organic carbon and pyrite sulfur in sediments over Phanerozoic time: a new theory. *Geochim. Cosmochim. Acta,* 47:855–862.

Ernst, W. G., and Calvert, S. E., 1969. An experimental study of the recrystallization of porcellanite and its bearing on the origin of some bedded cherts. *Am. J. Sci.,* 267A:114–133.

Heath, G. R., and Moberly, R., Jr., 1971. Cherts from the western Pacific, Leg 7, Deep Sea Drilling Project. *In* Winterer, E. L., Reidel, W. R., et al., *Init. Repts. DSDP,* 7 (Pt. 2): Washington (U.S. Govt. Printing Office), 991–1007.

Iijima, A., and Tada, R., 1990. Evolution of Tertiary sedimentary basins of Japan in reference to opening of the Japan Sea. *J. Fac. Sci. Univ. Tokyo, Sec. II,* 22:121–171.

Iijima, A., Tada, R., and Watanabe, Y., 1988. Developments of Neogene sedimentary basins in the northeastern Honshu Arc with emphasis on Miocene siliceous deposits. *J. Fac. Sci. Univ. Tokyo, Sec. II,* 21:417–446.

Inoue, A., Minato, H., and Utada, M., 1978. Mineralogical properties and occurrence of illite/montmorillonite mixed layer minerals formed from Miocene volcanic glass in Waga-Omono district. *Clay Sci.,* 5:123–126.

Inoue, K., and Naruse, T., 1987. Physical, chemical, and mineralogical characteristics of modern eolian dust in Japan and rate of dust deposition. *Soil Sci. Plant Nutr.,* 33:327–345.

Lancelot, Y., 1973. Chert and silica diagenesis in sediments from the Central Pacific. *In* Winterer, E. L., Ewing, J. I., et al., *Init. Repts. DSDP,* 17: Washington (U.S. Govt. Printing Office), 377–405.

Matsumoto, R., and Urabe, T., 1980. An automatic analysis of major elements in silicate rocks with X-ray fluorescence spectrometer using fused disc samples. *J. Jpn. Assoc. Min. Petr. Econ. Geol.,* 76:111–121.

Mizota, C., and Matsuhisa, Y., 1985. Eolian additions to soils and sediments of Japan. *Soil Sci. Plant Nutr.,* 28:38–54.

Murata, K. J., and Nakata, J. K., 1974. Cristobalitic stage in the diagenesis of diatomaceous shale. *Science,* 184:567–568.

Rea, D. K., Leinen, M., and Janecek, T. R., 1985. Geologic approach to the long-term history of atmospheric circulation. *Science,* 227:721–725.

Savrda, C. E., and Bottjer, D. J., 1986. Trace-fossil model for reconstruction of paleo-oxygenation in bottom waters. *Geology,* 14:3–6.

————, 1989. Trace-fossil model for reconstructing oxygenation histories of ancient marine bottom waters: application to Upper Cretaceous Niobrara Formation, Colorado. *Palaeogeogr., Palaeoclimatol., Palaeoecol.,* 74:49–74.

Sudo, T., 1974. *Clay Mineralogy:* Tokyo (Iwanami).

Tada, R., 1991a. Compaction and cementation in siliceous rocks and their possible effect on bedding enhancement. *In* Einsele, G., Ricken, W., and Seilacher, A. (Eds.), *Cycles and Events in Stratigraphy:* Heidelberg (Springer), 480–491.

————, 1991b. Origin of rhythmical bedding in middle Miocene siliceous rocks of the Onnagawa Formation, northern Japan. *J. Sediment. Petrol.,* 61:1123–1145.

Tada, R., and Iijima, A., 1983. Petrology and diagenetic changes of Neogene siliceous rocks in northern Japan. *J. Sediment. Petrol.,* 53:911–930.

Tamaki, K., Pisciotto, K., Allan, J., et al., 1990. *Proc. ODP, Init. Repts.,* 127: College Station, TX (Ocean Drilling Program).

Tsunogai, S., Suzuki, T., Kurata, T., and Uematsu, M., 1985. Seasonal and areal variation of continental aerosol in the surface air over the western North Pacific region. *J. Oceanogr. Soc. Jpn.,* 41:427–434.

Date of initial receipt: 21 March 1991
Date of acceptance: 12 December 1991
Ms 127/128B-188

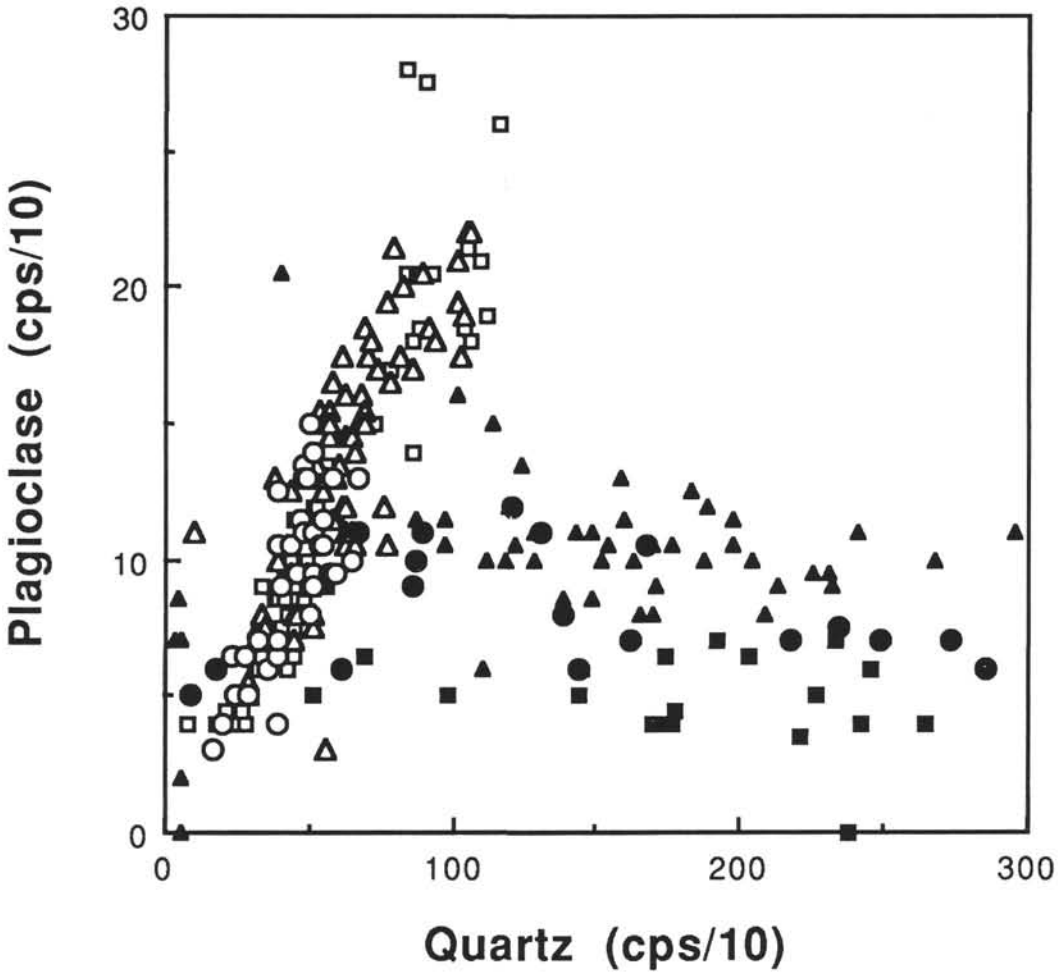

Figure 11. Relationship between the peak heights of quartz and plagioclase for samples from Sites 794 (squares), 795 (triangles), and 797 (circles). Open symbols are from the opal-A and opal-CT zones and solid symbols are from the quartz zone.

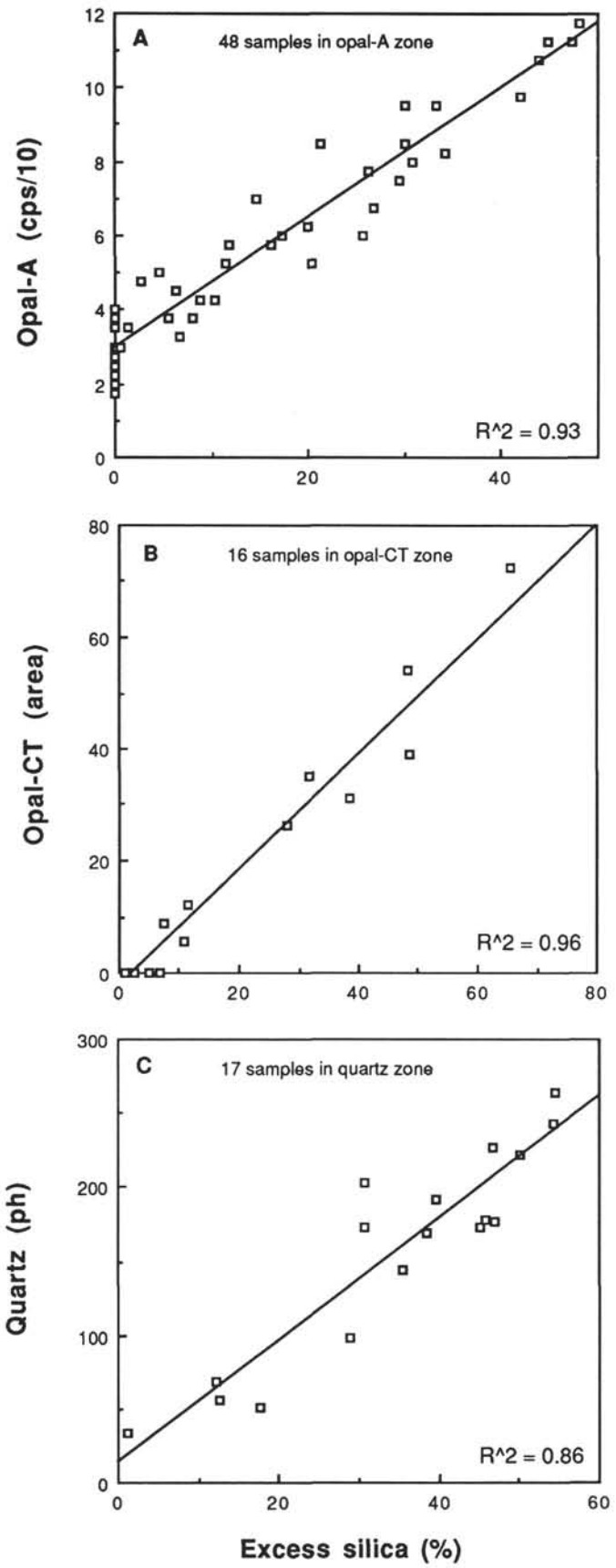

Figure 12. Relationships between the amount of excess silica estimated from the chemical composition and the peak height of opal-A (**A**), peak area of opal-CT (**B**), and peak height of quartz (**C**) for samples from Site 794.

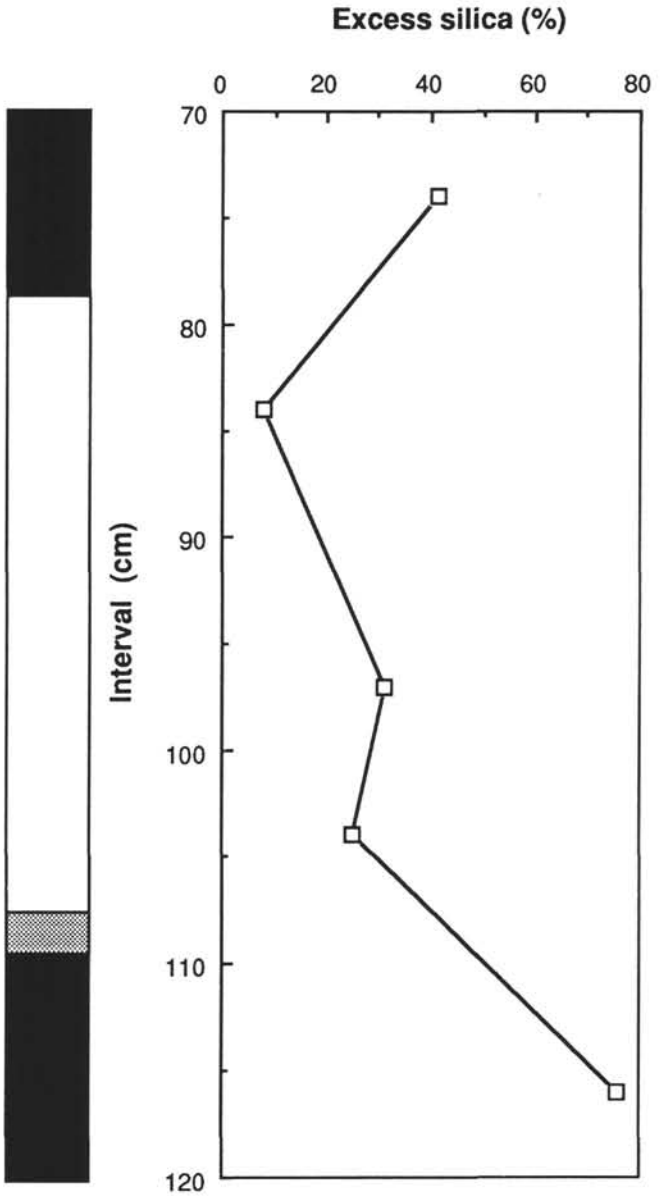

Figure 13. Vertical profile of excess silica content across a typical dark-light cycle in Unit 3 (Section 127-795C-9R-2, 73–117 cm). The interval is also pictured in Plate 2.

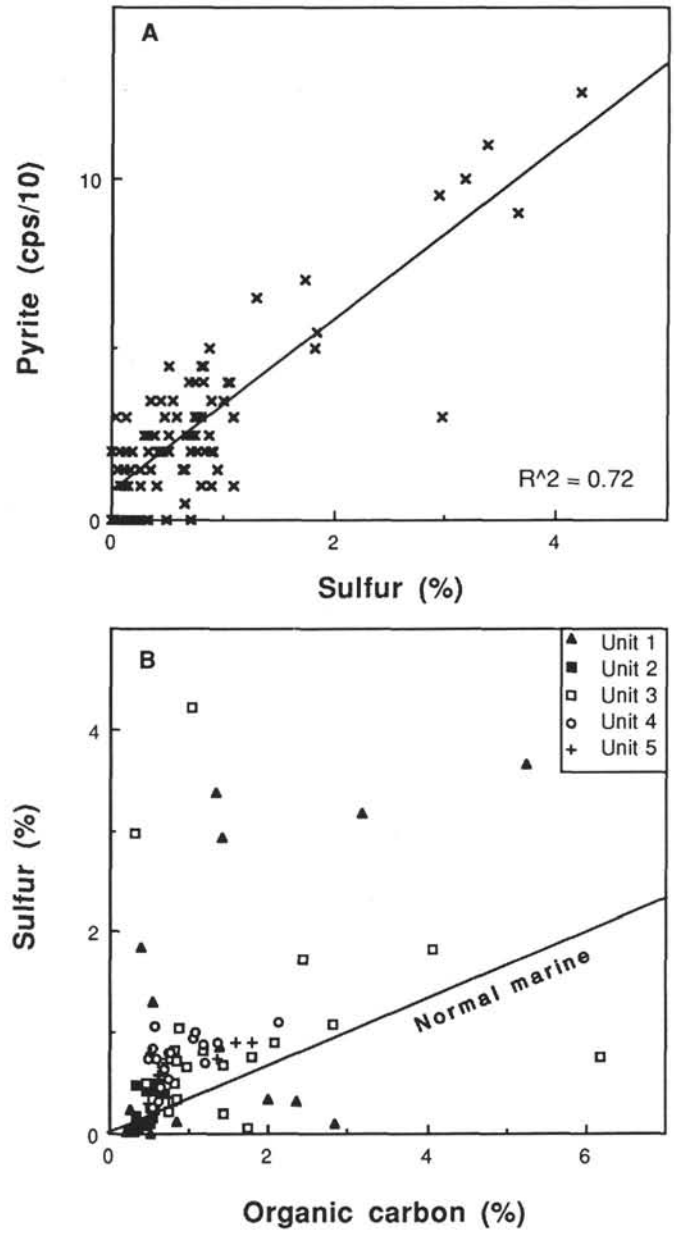

Figure 14. Relationships between total sulfur and pyrite peak height (**A**) and organic carbon and total sulfur (**B**). The line in Figure 14B represents the organic carbon/sulfur ratio of 3, which is typical for recent normal marine sediments according to Berner and Raiswell (1983).

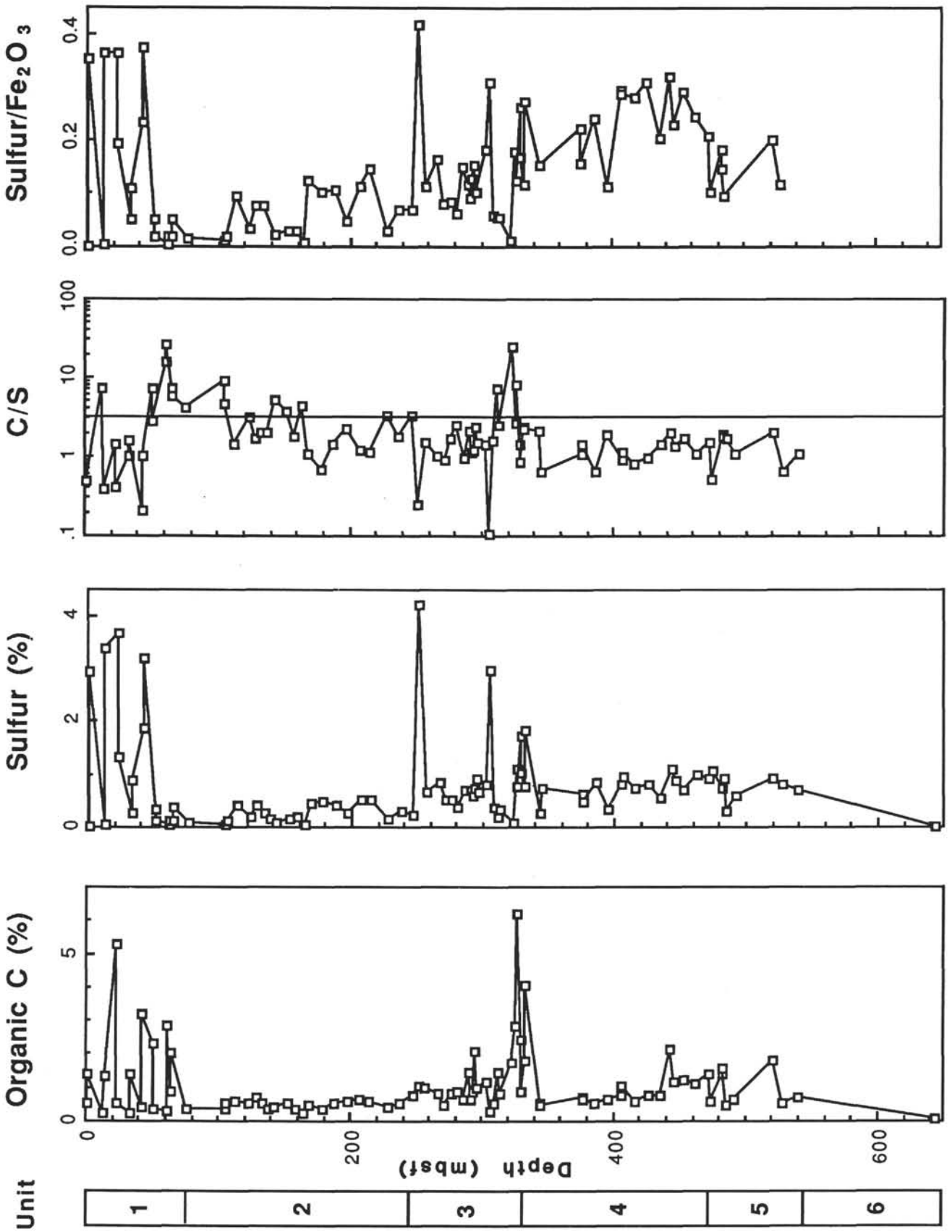

Figure 15. Vertical profiles of organic carbon and sulfur contents and C/S and S/Fe_2O_3 ratios for samples from Site 794.

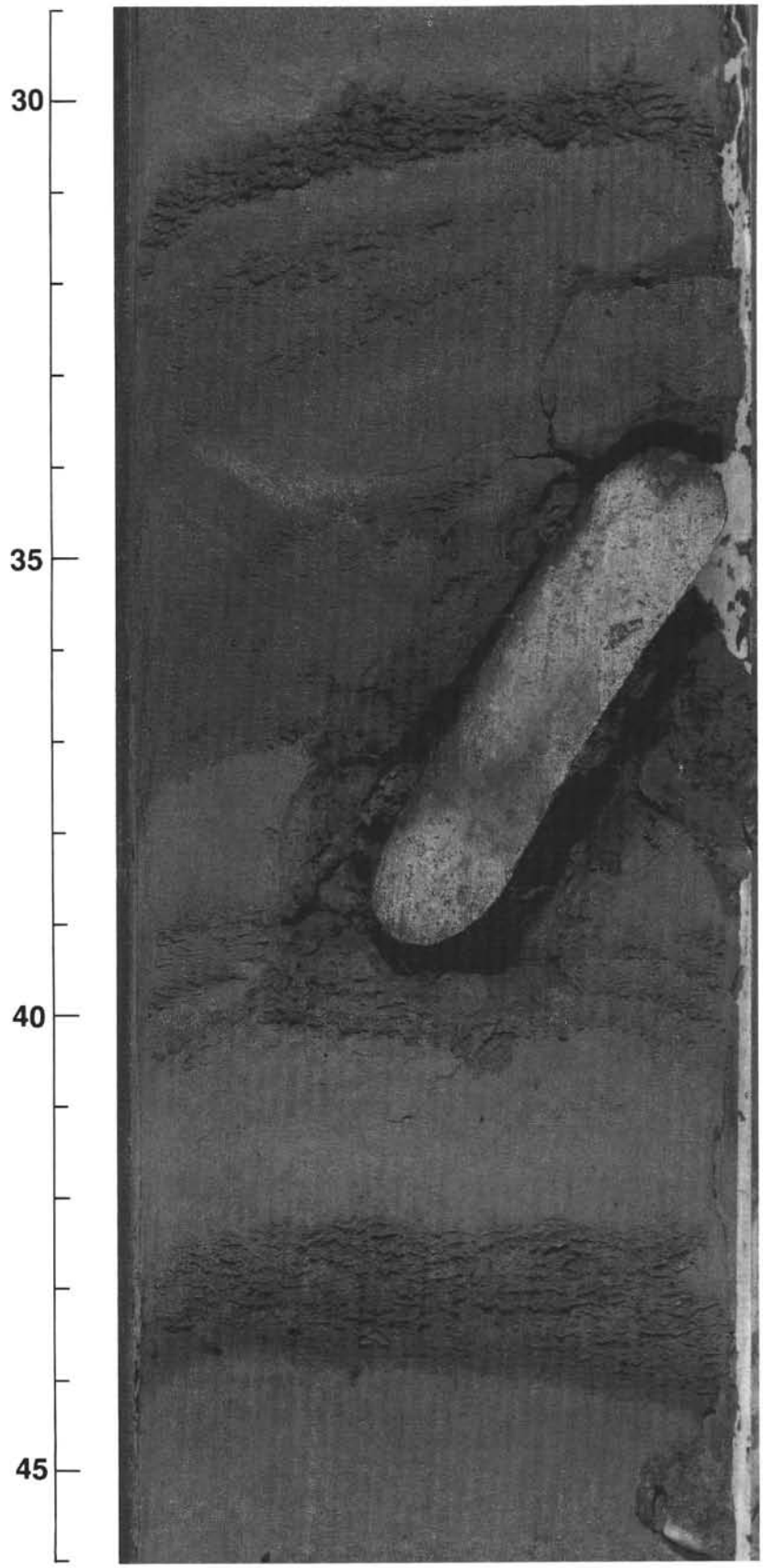

Plate 1. A dropstone within the hemipelagic sediments of Subunit 1A (Section 127-795A-2H-1, 29-46 cm).

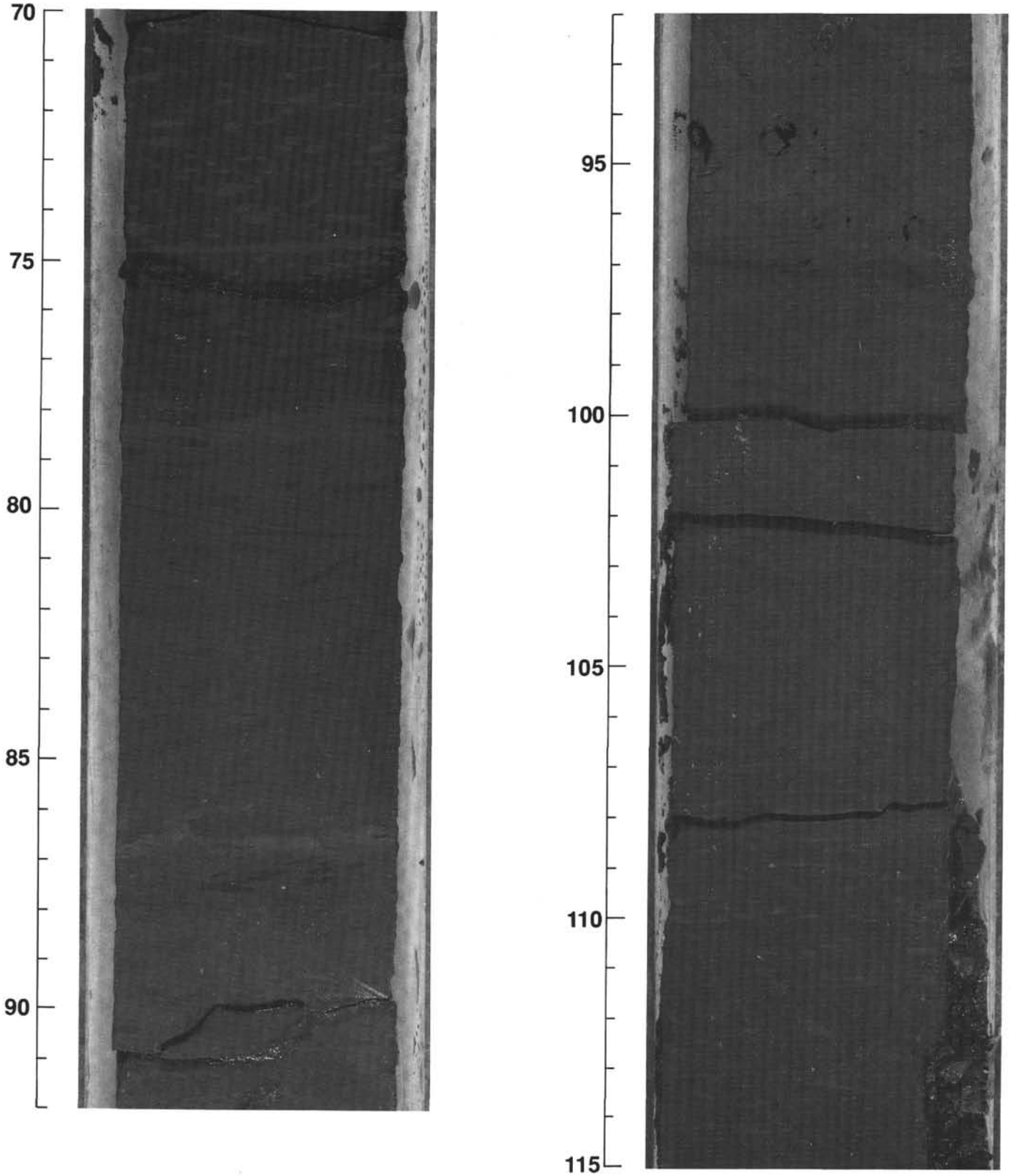

Plate 2. A typical dark-light cycle within the siliceous claystone of Unit 3 (Section 127-795C-9R-2, 70–115 cm).

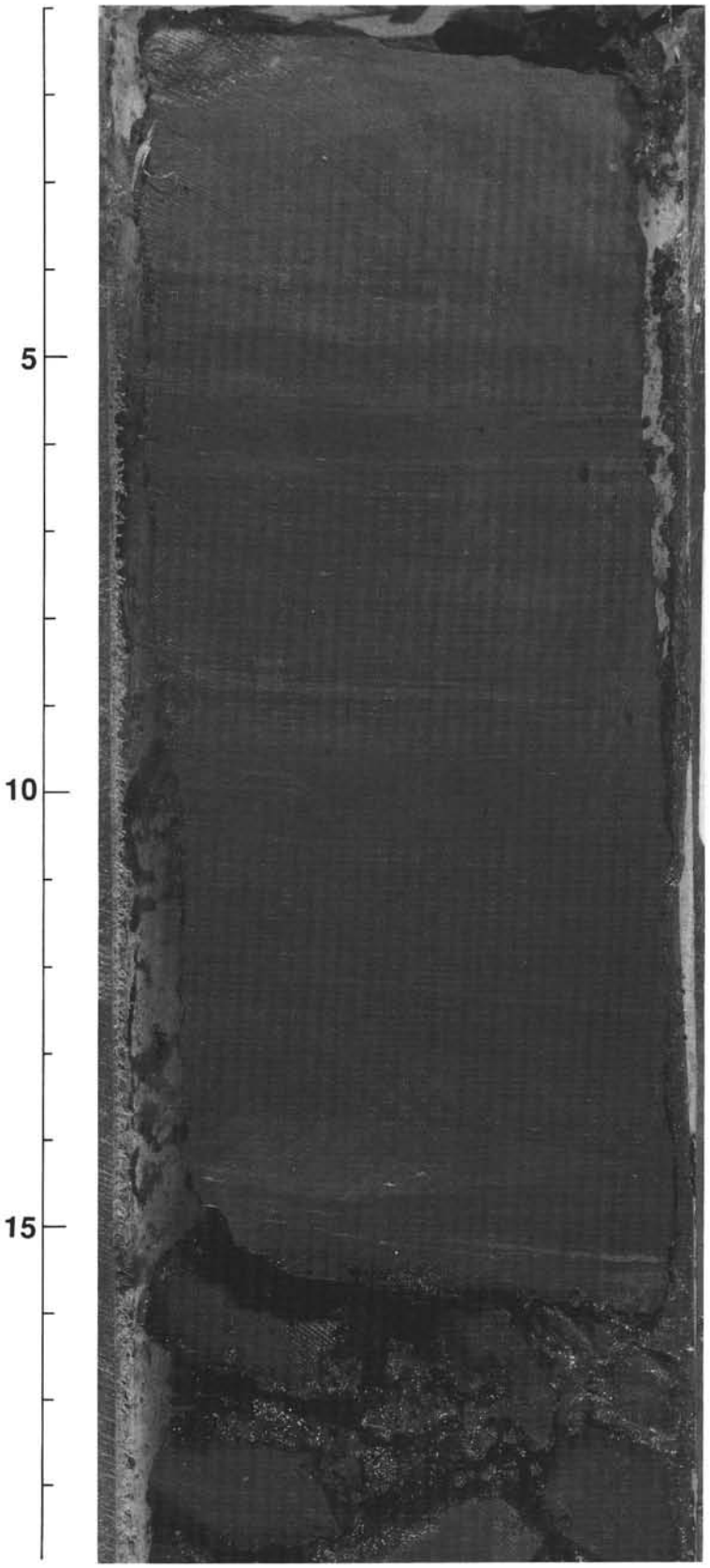

Plate 3. Siliceous claystone of Subunit 4B with horizontal burrows and parallel laminations (Section 127-794B-16R-3, 1-19 cm).

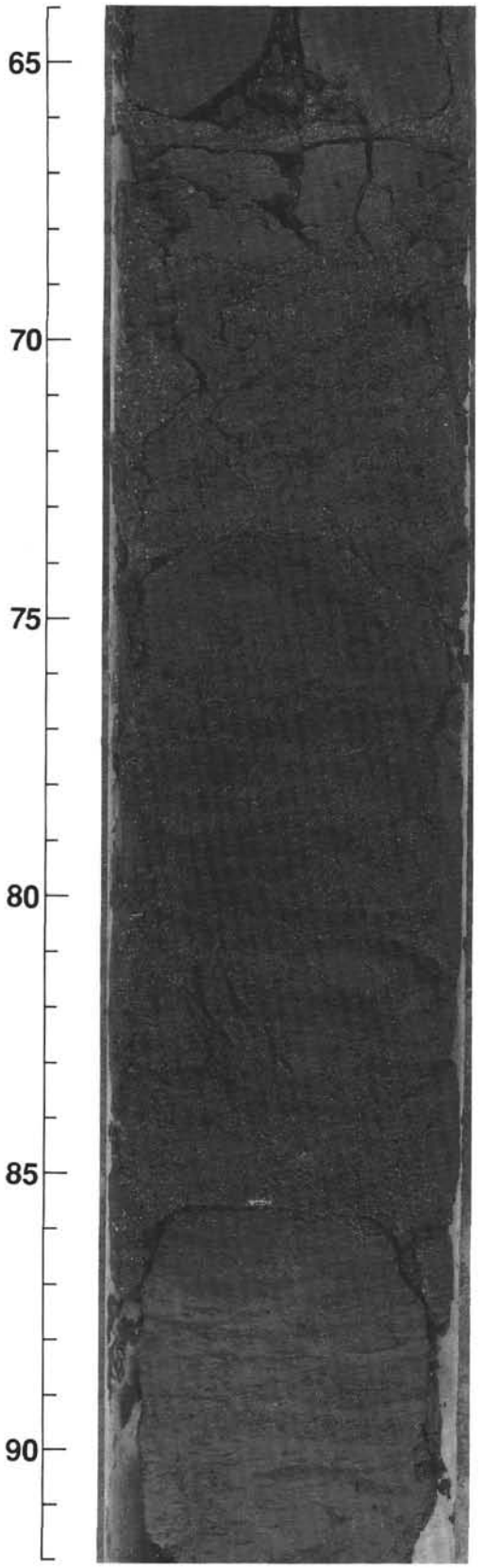

Plate 4. Glauconite bed at the base of Subunit 4B (Section 127-794B-19R-2, 64-92 cm).

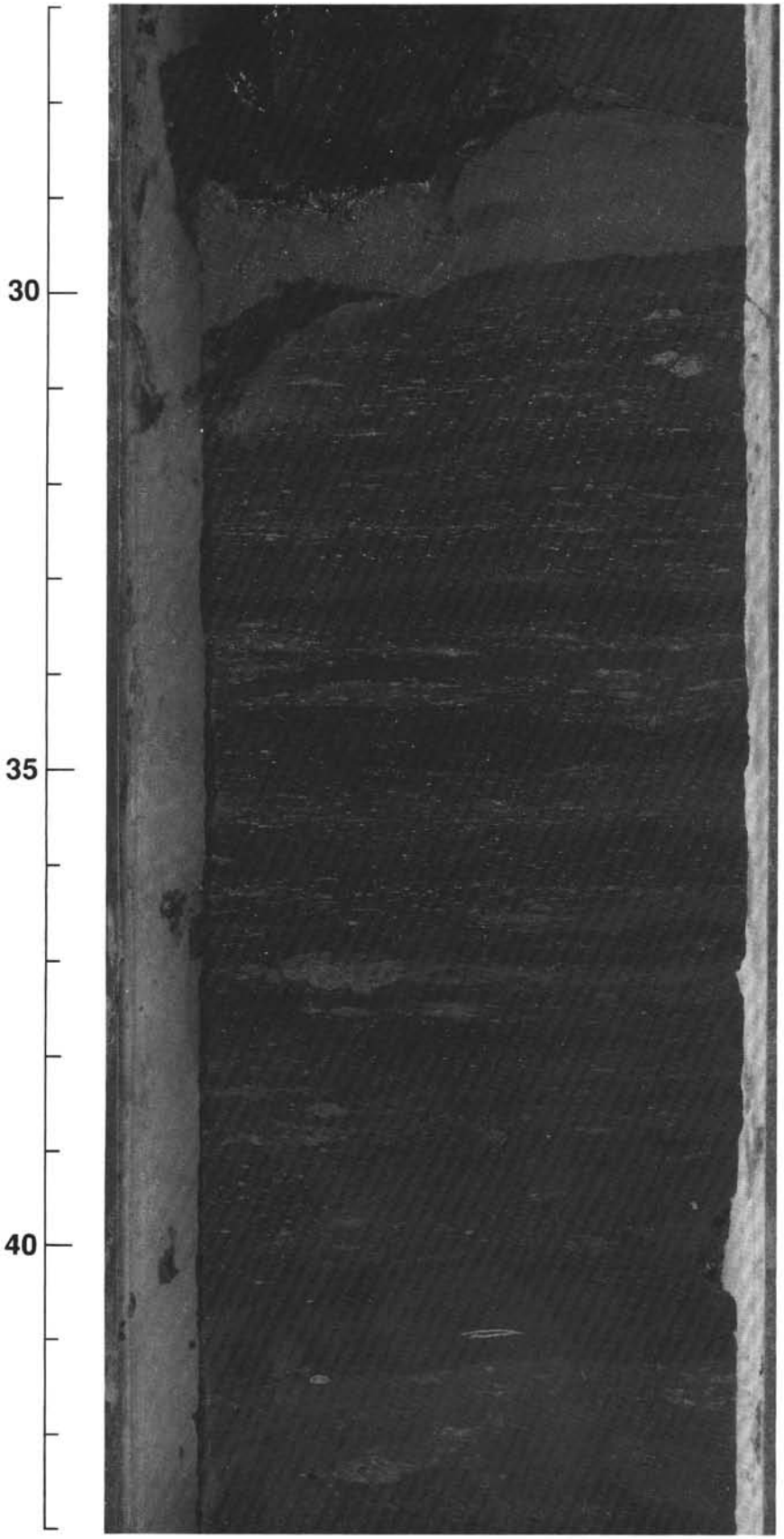

Plate 5. Claystone of Unit 5 with wispy carbonate laminae cut by horizontal burrows (Section 127-796B-33R-2, 27-43 cm).